SIAM J. Applied Dynamical Systems
Vol. 6, No. 4, pp. 694–727
© 2007 Society for Industrial and Applied Mathematics

# The Onset of Oscillations in Microvascular Blood Flow*

John B. Geddes†, Russell T. Carr‡, Nathaniel J. Karst†, and Fan Wu‡

**Abstract.** We explore the stability of equilibrium solution(s) of a simple model of microvascular blood flow in a two-node network. The model takes the form of convection equations for red blood cell concentration, and contains two important rheological effects—the Fåhræus–Lindqvist effect, which governs viscosity of blood flow in a single vessel, and the plasma skimming effect, which describes the separation of red blood cells at diverging nodes. We show that stability is governed by a linear system of integral equations, and we study the roots of the associated characteristic equation in detail. We demonstrate using a combination of analytical and numerical techniques that it is the relative strength of the Fåhræus–Lindqvist effect and the plasma skimming effect which determines the existence of a set of network parameter values which lead to a Hopf bifurcation of the equilibrium solution. We confirm these predictions with direct numerical simulation and suggest several areas for future research and application.

**Key words.** blood flow, microvascular network, instability, bifurcation

**AMS subject classifications.** 37-xx, 92-xx

**DOI.** 10.1137/060670699

## 1. Introduction.

Periodic or oscillatory dynamics in biological systems are common. Examples include the pacemaker in the heart, breathing patterns, and periodic fluctuations in leukocyte production in leukemia [15]. These types of phenomena require models consisting of nonlinear equations, most often in the form of nonlinear differential equations [14]. In fact, the modeling and analysis of complex physiological signals is a very active area for the application and development of dynamical systems theory [16].

Another example of fluctuating dynamics in biology is microvascular blood flow. Nobel prize winner August Krogh noted the heterogeneity of blood flow in the webbed feet of frogs in the early 1920's [24]. In *The Anatomy and Physiology of Capillaries* he wrote [23]

> In single capillaries the flow may become retarded or accelerated from no visible cause; in capillary anastomoses the direction of flow may change from time to time.

As more techniques were developed for measuring events in microcirculation, more fluctuations were reported. The servo-null pressure measurement system of Wiederhielm et al. [35] and Johnson and Wayland's [20] dual slit red cell velocity measurement device showed that

*Received by the editors September 25, 2006; accepted for publication (in revised form) by L. Fauci May 11, 2007; published electronically October 17, 2007. This work was supported in part by a grant from the National Institutes of Health (5 R01 HL067789-04), the undergraduate research opportunity program at the University of New Hampshire, and the Dean of Faculty's research fund at Olin College.
http://www.siam.org/journals/siads/6-4/67069.html
†Franklin W. Olin College of Engineering, Needham, MA 02492 (john.geddes@olin.edu, nathaniel.karst@students.olin.edu).
‡Department of Chemical Engineering, University of New Hampshire, Durham, NH 03824 (rtc@cisunix.unh.edu, fw@cisunix.unh.edu).



Copyright © by SIAM. Unauthorized reproduction of this article is prohibited.

fluctuations practically always occur in microvessels. These fluctuations are usually interpreted as evidence of "biological control" of the flow (precapillary sphincters, vasomotion, etc.). In fact the sine qua non cause for observed oscillations is often vasomotion [32].

However, oscillations may not be due solely to "biological control." In 1973 Y. C. Fung suggested that the observed dynamics might be due to statistical variations in the properties of cells and vessels [13]. Fung hypothesized that small stochastic variations in cell size or membrane stiffness could lead to apparently random fluctuations in flow and pressure in simple networks. He outlined a program of study of blood cell properties, vessel mechanics, blood rheology, and network geometry to be completed before his hypothesis could be tested; in many ways this research program is still active today [28].

The 1990's saw several attempts to apply the ideas of nonlinear dynamics to the microcirculation. Time series analysis of fluctuations suggested that the oscillations may be due to deterministic chaos. Yip, Nolstein-Rathlou, and Marsh [36] proposed that pressure oscillations in the kidney were due to nonlinearities in the tubuloglomerular feedback control mechanism including multiple time delays. Cavalcanti and Ursino [6] developed computer simulations of vasomotion in microvessels. They included both passive and active response to pressure which resulted in oscillations in vessel diameter or blood flow. Griffith [17] measured fluctuations in pressure and flow in the rabbit ear, again attributing vasomotion as the cause of the fluctuations. He also estimated the correlation dimension from the time series data to be between two and three and suggested that the dynamics were due to vasomotion control. More recently, Mollica, Jain, and Netti [26] interpreted the heterogeneity in tumor blood flow in terms of collapsible conduits for blood flow and Parthimos et al. [27] analyzed fluctuations in arteriol diameter and red cell velocity in the microcirculation of rats and measured small, positive Lyapunov exponents.

While the importance of vasomotion cannot be denied, there is growing evidence that fluctuations in microvascular blood flow can be due to inherent instabilities in the capillary network. Kiani et al. [21] found spontaneous oscillations in blood velocity in hamsters, even under experimental conditions which rule out myogenic or vasomotive effects. They also formulated a mathematical model of network blood flow and found good qualitative agreement with their experimental results. Their blood flow model is based on following slugs of red blood cells through the capillary network; the red blood cells move with a velocity which is determined by the hydraulic resistance of the network. In a network consisting of almost four hundred vessels (the topology and geometry were based on direct in vivo observations), spontaneous oscillations were found in 30% of them; the other vessels had steady flow and hematocrit.

Carr and LeCoin [4] reformulated the model as a system of partial differential equations for blood hematocrit. They found that blood velocity, hematocrit, and nodal pressures can oscillate spontaneously in the absence of biological control in small networks with about fifteen vessels. They found evidence of Hopf bifurcations and limit cycles but were unable to determine which parameters controlled the dynamics. In 2005, Carr, Geddes, and Wu [5] demonstrated that oscillations were possible in a network consisting of only two nodes and four vessels—the so-called two-node network. While the dimensionless parameters governing the onset of instability were discovered, finding unstable parameter values was an exercise in educated guessing. In addition, the influence of the various rheological properties of blood

Copyright © by SIAM. Unauthorized reproduction of this article is prohibited.

was poorly understood.

In this paper, we focus our attention on the two-node network and analyze in detail the onset of instability via Hopf bifurcation. In section 2 we review the major rheological properties of blood, including the Fåhræus–Lindqvist effect and the plasma skimming effect. We also introduce two simple, parametric models for these effects which make the analysis tractable. In section 3 we introduce the model of the two-node network and discuss the equilibrium solutions. In section 4 we derive the linearized equations close to steady state and the resulting characteristic equation that governs stability. In section 5 we show that Hopf bifurcations are possible, and we describe their dependence on three dimensionless parameters. In section 6 we develop a method for mapping the Hopf bifurcation points back to parameter space, thus allowing us to predict the network geometries that lead to instability, which we confirm via direct numerical simulation. We also investigate the relative importance of the Fåhræus–Lindqvist effect and the plasma skimming effect using two lumped parameters. Finally, in section 7 we offer some closing thoughts and remarks.

## 2. Blood rheology in microvessels.

Blood is a concentrated suspension containing red blood cells, white blood cells, and platelets. These components are suspended in plasma, an aqueous solution containing a variety of ions and macromolecules. We focus our attention on the red blood cells, which are biconcave discs with a typical diameter of about $8\mu m$ and thickness of $2\mu m$. Normal blood has a volume concentration of red blood cells (hematocrit) of about 45%.

The microcirculation consists of vessels with diameters ranging from $10\mu m$ to $100\mu m$, and is responsible for heat and mass exchange with the surrounding tissues; every cell in the body is within $100\mu m$ of a capillary. In this section we review two important rheological effects which we include in our model. The Fåhræus–Lindqvist effect captures the hematocrit- and diameter-dependent viscosity of blood when flowing through a single vessel. The plasma skimming effect describes the way red blood cells are distributed at a diverging node. We also propose two simple parametric versions of these which we use in this study in order to make the analysis tractable.

### 2.1. The Fåhræus–Lindqvist effect.

In the mid-nineteenth century, Jean Leonard Marie Poiseuille turned from his studies on the microcirculation of the frog to a series of detailed experiments on the flow of liquids in small glass capillaries [33]. Poiseuille demonstrated experimentally that the resistance to flow, defined as the ratio of the pressure drop to the volumetric flow rate, in a glass tube of circular cross-section is proportional to the length of the tube and inversely proportional to the fourth power of the diameter. In modern notation, Poiseuille's law reads

$$R = \frac{128 L \mu}{\pi D^4},$$

where $R$ is the resistance to flow, $D$ is the diameter of the tube, $L$ is the length of the vessel, and the constant of proportionality $\mu$ is a measure of the viscosity of the fluid. The first theoretical derivation of Poiseuille's law seems to have been published in 1860 by Hagenbach, but numerous authors appear to have made similar derivations during the same time period [33].

In 1931 Fåhræus and Lindqvist [11] conducted a set of experiments on blood flow through narrow capillary tubes with diameters ranging from $30\mu m$ to $300\mu m$. They demonstrated

Copyright © by SIAM. Unauthorized reproduction of this article is prohibited.

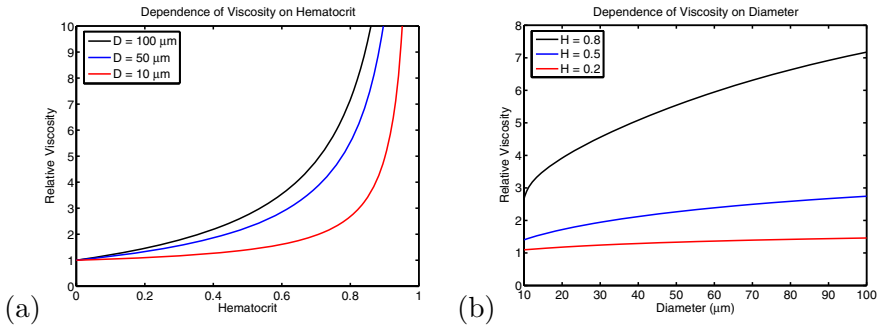


**Figure 1.** *Relative viscosity as a function of hematocrit and diameter from* (2.1)–(2.3). (a) *Viscosity dependence on hematocrit for diameters of* $10\mu m$, $50\mu m$, *and* $100\mu m$. (b) *Viscosity dependence on diameter for hematocrit values of* $H = 0.2$, $H = 0.5$, *and* $H = 0.8$.

that the viscosity of blood, computed according to Poiseuille's law, decreases with decreasing tube diameter, and they hypothesized that this was due to the red blood cells acting as a suspension. While not explicitly remarked upon in their paper, the viscosity of blood also depends upon hematocrit.

The dependence of blood viscosity on tube diameter (and hematocrit) has been confirmed by numerous investigators. In an empirical tour de force, Pries, Neuhaus, and Gaehtgens [30] compiled a database of viscosity measurements in tubes with diameters ranging from $3\mu m$ to $2000\mu m$ and with a range of hematocrits from 0 to 0.93. They also conducted a new set of experiments using a capillary viscometer and combined all of the data into an empirical relationship for the relative viscosity of blood $\mu(H, D)$,

$$\mu(H, D) = 1 + (\mu_{0.45} - 1)\frac{(1-H)^C - 1}{(1-0.45)^C - 1}, \tag{2.1}$$

where $H$ is the hematocrit and $\mu_{0.45}$ is the relative viscosity of blood at $H = 0.45$ which depends on diameter,

$$\mu_{0.45} = 220e^{-1.3D} + 3.2 - 2.44e^{-0.06D^{0.645}}. \tag{2.2}$$

The parameter $C$ also depends on diameter according to

$$C = \frac{1}{1 + 10^{11}D^{12}} + (0.8 + e^{-0.075D})\left(-1 + \frac{1}{1 + 10^{11}D^{12}}\right), \tag{2.3}$$

and in both cases $D$ is measured in microns. An example of the relative viscosity dependence on hematocrit is shown in Figure 1a for diameter values of $10\mu m$, $50\mu m$, and $100\mu m$. Notice that in each case the relative viscosity is unity at zero hematocrit and increases monotonically with increasing hematocrit and that increasing the diameter leads to an increase in relative viscosity. An example of the relative viscosity dependence on diameter is shown in Figure 1b for diameters in the range of $10\mu m$ to $100\mu m$ and hematocrit values of $H = 0.2$, $H = 0.5$, and $H = 0.8$.

Copyright © by SIAM. Unauthorized reproduction of this article is prohibited.

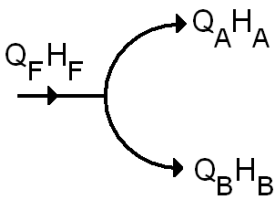


**Figure 2.** *Diverging node. The feed vessel has diameter $D_F$, flow $Q_F$, and hematocrit $H_F$. Daughter vessels $A$ and $B$ have diameters $D_A$ and $D_B$, flows $Q_A$ and $Q_B$, and hematocrits $H_A$ and $H_B$, respectively.*

**2.2. The plasma skimming effect.** August Krogh introduced the term plasma skimming in 1921 in order to explain the disproportionate distribution of red blood cells observed at microvascular bifurcations in vivo [24]. In the absence of plasma skimming, the hematocrit entering a side branch would equal that of the feed vessel, or, alternatively, the flow ratio of red blood cells entering a side branch would equal the volumetric flow ratio. Numerous authors, however, have demonstrated both in vitro and in vivo that the red blood cell flow ratio is a nonlinear function of the volumetric flow ratio which implies that the hematocrit ratio is not unity but depends on the volumetric flow ratio. In order to be clear, consider the diverging bifurcation shown in Figure 2, which consists of a feed vessel $F$ and two daughter vessels $A$ and $B$. Denote the hematocrit and flow in the feed and daughter vessels as $H_F$, $Q_F$, $H_A$, $Q_A$, $H_B$, and $Q_B$, respectively. In general, the hematocrit ratio $H_A/H_F$ is a function of the flow ratio $Q = Q_A/Q_F$ and is parameterized by the feed hematocrit $H_F$ and the diameters of the vessels $D_F$, $D_A$, and $D_B$ [12].

Many attempts to derive or measure the so-called plasma skimming function have been made. In vitro studies using plastic particles were conducted by Bugliarello and Hsiao [3] and Chien et al. [7], while Dellimore, Dunlop, and Canham [8] and Fenton, Carr, and Cokelet [12] conducted in vitro experiments using human blood. Klitzman and Johnson [22] performed in vivo experiments using hamsters, while Pries, Ley, and Gaehtgens [29] examined the distribution of red cells at sixty-five arteriol bifurcations in the rat mesentry. Some general conclusions can be drawn from these studies: red cells are not distributed in proportion to the volume flow; there is a critical fractional flow, $Q_0$, to a side branch below which the latter receives no blood cells; and side branch hematocrit is not always equal to feed hematocrit for $Q = 0.5$. Pries, Ley, and Gaehtgens [29] fitted experimental data to the piecewise plasma skimming function

$$\frac{H_A Q_A}{H_F Q_F} = \begin{cases} 0, & Q < Q_0, \\ \frac{e^r (Q-Q_0)^p}{e^r (Q-Q_0)^p + (1-Q-Q_0)^p}, & Q_0 \le Q \le 1 - Q_0, \\ 1, & Q > 1 - Q_0, \end{cases} \tag{2.4}$$

and determined the dependence of the dimensionless fitting parameters on the network parameters as

$$r = -\frac{6.96}{D_F} \ln\left(\frac{D_A}{D_B}\right),$$

Copyright © by SIAM. Unauthorized reproduction of this article is prohibited.

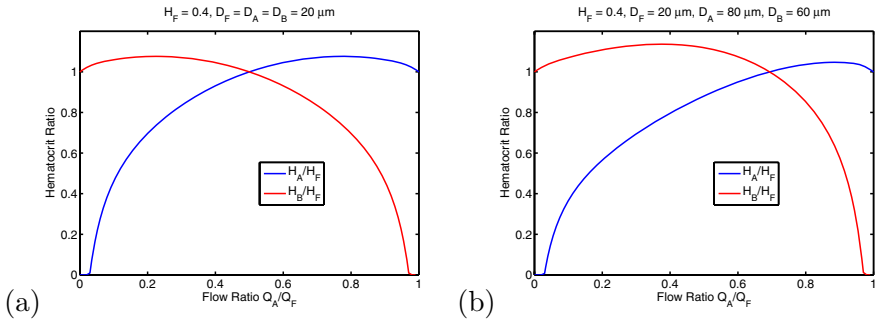


**Figure 3.** *Plasma skimming function from* (2.4). (a) $H_F = 0.4$, $D_F = D_A = D_B = 20\mu m$. (b) $H_F = 0.4$, $D_F = 20\mu m$, $D_A = 80\mu m$, $D_B = 60\mu m$.

$$p = 1 + 6.98\frac{(1 - H_F)}{D_F},$$
$$Q_0 = \frac{0.4}{D_F},$$

where all of the diameters are measured in microns. More recently, Enden and Popel [10] conducted three-dimensional simulations of flow in a T-type bifurcation and found good agreement with the various experimental studies mentioned above.

In Figure 3 we plot Pries, Ley, and Gaehtgens's plasma skimming function for a couple of different parameter values in order to highlight the key features. We choose to plot the hematocrit ratio as a function of flow ratio for reasons that will become clear in future sections. Figure 3a shows both the hematocrit ratio in branch $A$ and the hematocrit ratio in branch $B$ as functions of the flow ratio $Q = Q_A/Q_F$ for the following parameter values: $H_F = 0.4$, $D_F = 20\mu m$, and $D_A = D_B = 20\mu m$. As a result of the equal diameters in the daughter branches, the parameter $r = 0$, which implies that the hematocrit ratio in both branches is unity for $Q = 0.5$. In addition, there is a critical flow rate of $Q_0 = 0.02$ below which there is no hematocrit entering branch $A$ and a similar value for branch $B$. For this symmetric set of parameters, the hematocrit ratio in branch $B$ is simply obtained by reflection about the $Q = 0.5$ axis. Note that there is a discontinuity in the derivative of either function at $Q_0$ and $1 - Q_0$. In Figure 3b we show the plasma skimming function in each branch for a nonsymmetric bifurcation. The parameter values are $H_F = 0.4$, $D_F = 20\mu m$, $D_A = 80\mu m$, and $D_B = 60\mu m$. The nonequal daughter branches mean that the parameter $r \neq 0$, which breaks the symmetry of the plasma skimming functions about $Q = 0.5$. Although the plasma skimming functions are no longer mirror images, red blood cell flow is still conserved; i.e.,

$$Q_F H_F = Q_A H_A + Q_B H_B. \tag{2.5}$$

**2.3. Parametric models.** The empirical models of Pries et al. [29, 30] provide a detailed description of the dependence of viscosity and plasma skimming on the various vessel and flow parameters. In order to gain insight, however, we propose using simple parametric models for the Fåhræus–Lindqvist effect and plasma skimming effect as follows. We assume the viscosity has an exponential dependence on hematocrit,

$$\mu(H) = e^{\delta H}, \tag{2.6}$$

Copyright © by SIAM. Unauthorized reproduction of this article is prohibited.

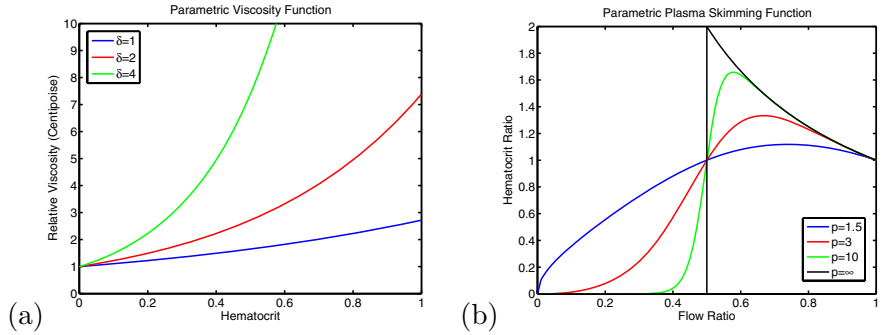


**Figure 4.** *Simple parametric models.* (a) *Exponential viscosity model.* (b) *Logit plasma skimming model.*

where $\delta$ is an adjustable parameter. In what follows we will assume that the same $\delta$ applies in any branch. In Figure 4a we plot the exponential function for three different values of $\delta$. This parametric model captures the relevant feature of the Pries et al. viscosity model, namely, that viscosity is a monotonically increasing function of hematocrit with $\mu(0) = 1$. The choice of an exponential model is not unreasonable: the viscosity model of Pries, Neuhaus, and Gaehtgens [30] demonstrates a strong dependence on hematocrit; we have used other monotonically increasing models and find no substantial differences in the results that follow; and, perhaps most importantly, the exponential model makes the analysis tractable.

It is also impossible to capture all of the features of the plasma skimming function with only a single parameter. However, Carr, Geddes, and Wu [5] showed that the key ingredient is the existence of a maximum. We will use a semiempirical model proposed by Klitzman and Johnson [22],

$$\frac{H_A Q_A}{H_F Q_F} = \frac{Q^p}{Q^p + (1-Q)^p}, \tag{2.7}$$

where $p > 1$ is an adjustable parameter and $Q \in [0, 1]$. This model does not have a critical flow rate, nor does it give rise to nonsymmetric plasma skimming functions. It does, however, have a single maximum. Increasing the value of $p$ leads to very low values of hematocrit for low values of $Q$ while also leading to an increase in the maximum hematocrit. In Figure 4b we plot the hematocrit ratio as a function of flow ratio for several different values of $p$. Note that increasing $p$ leads to a greater maximum value which slowly shifts toward $Q = 0.5$. In the limit as $p \to \infty$, the plasma skimming function is piecewise continuous and behaves as $1/Q$ for $Q \geq 0.5$.

**3. The two-node network model.** The model which we use was first proposed by Kiani et al. [21] and later reformulated by Carr and LeCoin [4]. It is a continuous model and assumes that the essence of microvascular blood flow can be captured with a position- and time-dependent hematocrit function. It is therefore a one-dimensional model and ignores the three-dimensional aspect of the problem and the discrete nature of red blood cells. In sections 3.1 and 3.2 we describe the partial differential equation model and relevant boundary conditions, while in section 3.3 we prove that there exists at least one equilibrium solution of the model, and we also find conditions under which there are multiple equilibria.

Copyright © by SIAM. Unauthorized reproduction of this article is prohibited.

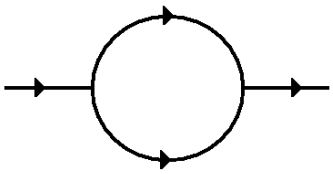

**Figure 5.** *The two-node network consists of a single inlet and a single outlet.*

**3.1. The PDE model.** Consider the simple two-node network shown in Figure 5. We assume that the hematocrit in each branch is governed by a first-order wave equation of the form

$$\frac{\partial H_A}{\partial t} + v_A \frac{\partial H_A}{\partial x_A} = 0, \qquad 0 \le x_A \le l_A, \quad t \ge 0,$$
$$\frac{\partial H_B}{\partial t} + v_B \frac{\partial H_B}{\partial x_B} = 0, \qquad 0 \le x_B \le l_B, \quad t \ge 0,$$

where $H_A(x_A, t)$ and $H_B(x_B, t)$ are the hematocrits in branches $A$ and $B$, respectively. This is an appropriate description for the one-dimensional transport of red cells with small dispersion. The propagation velocity in each branch is proportional to the flow in each branch

$$v_A(t) = \frac{4Q_A(t)}{\pi d_A^2},$$
$$v_B(t) = \frac{4Q_B(t)}{\pi d_B^2},$$

where $Q_A$ and $Q_B$ are the flows in branches $A$ and $B$, respectively, and $d_A$ and $d_B$ are the diameters of branches $A$ and $B$, respectively. It is possible to express both velocities in terms of the fractional flow in branch $A$, $Q(t) = Q_A(t)/Q_F$, where $Q_F$ is the steady volumetric flow rate in the feed branch. Conservation of volumetric flow at the branch implies that $Q_A(t) + Q_B(t) = Q_F$. It also implies that $0 \le Q(t) \le 1$.

A dimensionless form of the governing equations may be derived by scaling space and time according to

$$\hat{x}_A = \frac{x_A}{l_A},$$
$$\hat{x}_B = \frac{x_B}{l_B},$$
$$\hat{t} = t\frac{4Q_F}{\pi d_A^2 l_A},$$

which results in the following dimensionless propagation equations:

$$\frac{\partial H_A}{\partial t} + Q\frac{\partial H_A}{\partial x_A} = 0, \qquad 0 \le x_A \le 1, \quad t \ge 0, \tag{3.1}$$

$$\frac{\partial H_B}{\partial t} + \alpha(1-Q)\frac{\partial H_B}{\partial x_B} = 0, \qquad 0 \le x_B \le 1, \quad t \ge 0. \tag{3.2}$$

Copyright © by SIAM. Unauthorized reproduction of this article is prohibited.

The hats have been dropped for convenience and the parameter $\alpha$ has been introduced. It is the ratio of the volume of branch $A$ to that of branch $B$,

$$\alpha = \frac{l_A d_A^2}{l_B d_B^2}.$$

The propagation velocity in branch $A$ is now $Q$, while in branch $B$ the velocity is $\alpha(1-Q)$.

**3.2. Constitutive relations and boundary conditions.** The governing equations, (3.1)–(3.2), are accompanied by constitutive relations and boundary conditions. Conservation of flow and the two-node network topology determine the fractional flow rate in branch $A$ in terms of the hydraulic resistance of each branch,

$$Q(t) = \frac{R_B(t)}{R_A(t) + R_B(t)}, \tag{3.3}$$

with a similar expression for branch $B$. In turn, the hydraulic resistance in each branch is determined by the Fåhræus–Lindqvist effect,

$$R_A(t) = \frac{128 l_A}{\pi d_A^4} \mu_A(\bar{H}_A(t), d_A), \tag{3.4}$$

$$R_B(t) = \frac{128 l_B}{\pi d_B^4} \mu_B(\bar{H}_B(t), d_B), \tag{3.5}$$

where $\mu_A$ and $\mu_B$ are the relative viscosities in branches $A$ and $B$, respectively. The viscosity in each branch is a function of the axially averaged hematocrit in the branch and the diameter of the branch. Finally, the entrance hematocrit to each branch is governed by the plasma skimming effect,

$$H_A(0,t) = H_F f(Q(t)), \tag{3.6}$$

$$H_B(0,t) = H_F g(Q(t)), \tag{3.7}$$

where $H_F$ is the hematocrit of the feed branch, and the functions $f$ and $g$ specify the plasma skimming effect for branches $A$ and $B$, respectively. The governing equations (3.1)–(3.2), along with the constitutive relations (3.3)–(3.5) and boundary conditions (3.6)–(3.7), completely determine the problem.

**3.3. Equilibrium solutions.** In steady state, $\partial H_A/\partial t = 0$, the hematocrit along each branch is constant and equal to the entrance hematocrit. The entrance hematocrit depends on the steady state flow $Q^*$, which in turn implies that the steady state viscosity $\mu_A^*$ is a function of $Q^*$. The hydraulic resistance in each branch is therefore a function of $Q^*$ in steady state, and (3.3) becomes

$$Q^* = \psi(Q^*), \tag{3.8}$$

where the nonlinear function on the right-hand side may be written as

$$\psi(Q^*) = \frac{1}{1 + \frac{d_B^4 l_A \mu_A^*}{d_A^4 l_B \mu_B^*}}. \tag{3.9}$$

Copyright © by SIAM. Unauthorized reproduction of this article is prohibited.

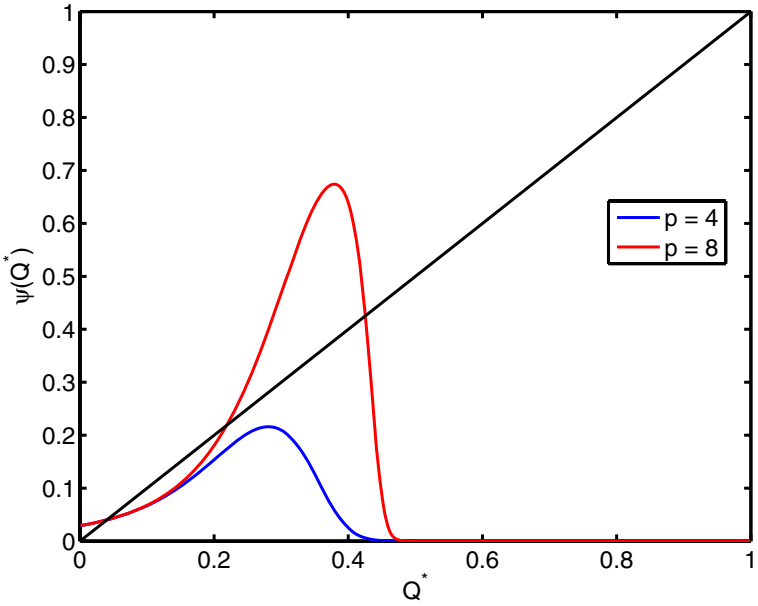


**Figure 6.** *Steady state solutions are given where the function $\psi$, defined in (3.9), crosses the line of unit slope. The parameter values are $\delta H_F = 8$, $l_A/l_B = 10$, and $d_B/d_A = 10$. For $p = 4$ there is one steady state solution, while for $p = 8$ there are three steady state solutions.*

The steady state viscosity is determined via the relations

$$\mu_A^* = \mu_A(\bar{H}_A^*, d_A), \tag{3.10}$$

$$\mu_B^* = \mu_B(\bar{H}_B^*, d_B), \tag{3.11}$$

$$\bar{H}_A^* = H_F f(Q^*), \tag{3.12}$$

$$\bar{H}_B^* = H_F g(Q^*). \tag{3.13}$$

We are now ready to state our first result concerning the existence of equilibrium solutions.

Theorem 3.1. *Assume that $\mu_A$ and $\mu_B$ are positive, continuous functions of $\bar{H}_A$ and $\bar{H}_B$. Also assume that $f$ and $g$ are continuous functions of $Q^*$. Then at least one steady state solution to (3.8)–(3.10) exists.*

*Proof.* We appeal to the Brouwer fixed-point theorem. If the viscosity functions are continuous functions of $\bar{H}_A$ and $\bar{H}_B$ and the plasma skimming functions are continuous functions of $Q^*$, then $\psi(Q^*)$ is continuous. In addition, the positivity of the viscosity functions implies that $\psi \in [0, 1]$ for all $Q^* \in [0, 1]$. By the fixed-point theorem this implies that at least one root exists with $Q^* \in [0, 1]$. ∎

A closed form solution for $Q^*$ cannot be obtained except in the case of simple viscosity models. Solutions can be visualized, however, by plotting $\psi(Q^*)$ versus $Q^*$ as demonstrated in Figure 6 for different parameter values. Equilibrium solutions are given where the function $\psi$ crosses the line of unit slope. Here we use the parametric models with the following parameter values: $\delta H_F = 8$, $l_A/l_B = 10$, and $d_B/d_A = 10$. Notice that while Theorem 3.1 guarantees that a root exists, it does not guarantee that it is unique. Indeed, Figure 6 demonstrates

Copyright © by SIAM. Unauthorized reproduction of this article is prohibited.

that, as we hold the value of $\delta H_F$ fixed and change from $p = 4$ to $p = 8$, we transition from a system with a single steady state to one with multiple steady states. We state and prove below a condition which guarantees that the steady state is unique.

Theorem 3.2. *Define two dimensionless parameters, $b$ and $c$, according to*

$$b = -H_F Q^*(1-Q^*) f'(Q^*) \frac{\mu_A'^*}{\mu_A^*},$$
$$c = H_F Q^*(1-Q^*) g'(Q^*) \frac{\mu_B'^*}{\mu_B^*}.$$

*The steady state solution is unique if and only if*

$$b + c < 1$$

*for all $Q^* \in (0,1)$. The derivative of $\mu_A$ with respect to the average hematocrit is*

$$\mu_A'^* = \left.\frac{\partial \mu_A}{\partial \bar{H}_A}\right|_{Q^*},$$

*while the derivative of $f$ with respect to the flow rate is*

$$f'(Q^*) = \left.\frac{df}{dQ}\right|_{Q^*}.$$

*Similar expressions apply to branch $B$.*

*Proof.* Since $Q^*$ is constrained to the closed interval $[0,1]$, we can rearrange (3.8) for the ratio of the lengths,

$$\frac{l_A}{l_B} = \left(\frac{d_A}{d_B}\right)^4 \left(\frac{1-Q^*}{Q^*}\right) \frac{\mu_B^*}{\mu_A^*}, \tag{3.14}$$

and use this formulation to determine whether the equilibrium solution is unique. The positive, continuous viscosity functions imply that $l_A/l_B \geq 0$ for all $Q^* \in [0,1]$ and that

$$\lim_{Q^* \to 0} \frac{l_A}{l_B} = +\infty,$$
$$\lim_{Q^* \to 1} \frac{l_A}{l_B} = 0.$$

The length ratio therefore cannot be a monotonically increasing function of $Q^*$. If $\frac{d(l_A/l_B)}{dQ^*} < 0$ for all $Q^* \in (0,1)$, then the length ratio is a monotonically decreasing function of $Q^*$, which implies that the steady state solution $Q^*$ is unique for any set of network parameters. The derivative is

$$\frac{d}{dQ^*}\left(\frac{l_A}{l_B}\right) = \frac{1}{Q^{*2}} \frac{\mu_B^*}{\mu_A^*} \left(\frac{d_A}{d_B}\right)^4 (b + c - 1),$$

thus proving that the equilibrium solution is unique if $b + c - 1 < 0$ for all $Q^*$. If, on the other hand, there exists a $Q^* \in (0,1)$ for which $\frac{d(l_A/l_B)}{dQ^*} > 0$, then, by continuity of $l_A/l_B$, there exists multiple equilibrium solutions for some set of network parameters. ∎

Copyright © by SIAM. Unauthorized reproduction of this article is prohibited.

**4. Linearized equations.** While the governing partial differential equations and accompanying constitutive relations are convenient for numerical simulation, they are not very useful from an analytical point of view. They can, however, be linearized and then transformed into a corresponding system of delay equations which can in turn be manipulated into a single linear integral equation. This proves to be most convenient in analyzing the linear stability of the steady state solution(s).

We begin by rewriting the governing partial differential equations (3.1)–(3.2) about the steady state solution. We assume that $Q(t) = Q^*$ for $t < 0$, $\bar{H}_A(t) = \bar{H}_A^*$, and $\bar{H}_B(t) = \bar{H}_B^*$ for $t \leq 0$. A perturbation will be introduced into the flow rate by specifying $Q(0) \neq Q^*$ and defining

$$\begin{aligned} Q(t) &= Q^* + \tilde{Q}(t), \\ H_A(x_A, t) &= \bar{H}_A^* + \tilde{H}_A(x_A, t), \\ H_B(x_B, t) &= \bar{H}_B^* + \tilde{H}_B(x_B, t). \end{aligned}$$

Replacing into (3.1)–(3.2) and grouping terms lead to the system of partial differential equations

$$\frac{\partial \tilde{H}_A}{\partial t} + Q^* \frac{\partial \tilde{H}_A}{\partial x_A} = -\tilde{Q} \frac{\partial \tilde{H}_A}{\partial x_A}, \tag{4.1}$$

$$\frac{\partial \tilde{H}_B}{\partial t} + \alpha(1 - Q^*) \frac{\partial \tilde{H}_B}{\partial x_B} = \alpha \tilde{Q} \frac{\partial \tilde{H}_B}{\partial x_B}. \tag{4.2}$$

If we drop the nonlinear terms on the right-hand side, then the linearized equations consist of two coupled, constant velocity propagation equations for perturbations to the equilibrium hematocrit. We can define the steady state propagation (or delay) times in branches $A$ and $B$, respectively, as

$$\begin{aligned} \tau^* &= \frac{1}{Q^*}, \\ \theta^* &= \frac{1}{\alpha(1 - Q^*)}. \end{aligned}$$

A more convenient form for analysis can be found by integrating (4.1)–(4.2) over the spatial variable in each branch,

$$\begin{aligned} \tau^* \frac{d\hat{H}_A}{dt} &= \tilde{H}_A(0, t) - \tilde{H}_A(1, t), \\ \theta^* \frac{d\hat{H}_B}{dt} &= \tilde{H}_B(0, t) - \tilde{H}_B(1, t), \end{aligned}$$

where $\hat{H}_A$ is defined by

$$\hat{H}_A(t) = \int_0^1 \tilde{H}_A(x_A, t)\, dx_A,$$

and similarly for $\hat{H}_B$. This implies that

$$\bar{H}_A(t) = \bar{H}_A^* + \hat{H}_A(t),$$

Copyright © by SIAM. Unauthorized reproduction of this article is prohibited.

with a similar expression for the other branch.

We now make use of the fact that our governing linearized equations are a pair of first-order wave equations with constant velocity. This implies that the hematocrit in each branch simply propagates along the appropriate characteristic with velocity $Q^*$ in branch $A$ and $\alpha(1-Q^*)$ in branch $B$. The hematocrit at the exit of vessel $A$ is therefore the hematocrit at the entrance at an earlier time, namely, $\tau^*$. With this in mind, the governing equations reduce to

$$\tau^* \frac{d\hat{H}_A}{dt} = \tilde{H}_A(0,t) - \tilde{H}_A(0,t-\tau^*),$$
$$\theta^* \frac{d\hat{H}_B}{dt} = \tilde{H}_B(0,t) - \tilde{H}_B(0,t-\theta^*).$$

Recall that the entrance hematocrit in branch $A$ is specified by the plasma skimming rule (3.6) which linearizes to give

$$\begin{aligned} & H_A(0,t) = H_F f(Q), \\ \Rightarrow\ & H_A(0,t) = H_F(f(Q^*) + f'(Q^*)\tilde{Q}), \\ \Rightarrow\ & \tilde{H}_A(0,t) = H_F f'(Q^*)\tilde{Q}, \end{aligned}$$

with a similar expression for branch $B$. Our linearized governing equations become

$$\tau^* \frac{d\hat{H}_A}{dt} = H_F f'(Q^*)\left(\tilde{Q}(t) - \tilde{Q}(t-\tau^*)\right),$$
$$\theta^* \frac{d\hat{H}_B}{dt} = H_F g'(Q^*)\left(\tilde{Q}(t) - \tilde{Q}(t-\theta^*)\right),$$

which is a pair of delay differential equations with constant delay. If we integrate each of these from $t=0$ to $t=T$ we find

$$\tau^* \hat{H}_A(T) = H_F f'(Q^*) \int_0^T \left(\tilde{Q}(s) - \tilde{Q}(s-\tau^*)\right) ds, \tag{4.3}$$

$$\theta^* \hat{H}_B(T) = H_F g'(Q^*) \int_0^T \left(\tilde{Q}(s) - \tilde{Q}(s-\theta^*)\right) ds, \tag{4.4}$$

where we have used the initial conditions $\hat{H}_A(0) = 0$ and $\hat{H}_B(0) = 0$. In addition, we can decompose the remaining integrals into two pieces,

$$\int_0^T \tilde{Q}(s-\tau^*)\, ds = \int_0^{\tau^*} \tilde{Q}(s-\tau^*)\, ds + \int_{\tau^*}^T \tilde{Q}(s-\tau^*)\, ds,$$

and use the initial condition on the flow perturbation to conclude that the first term is zero. A change of variables results in

$$\int_0^T \tilde{Q}(s-\tau^*)\, ds = \int_0^{T-\tau^*} \tilde{Q}(u)\, du.$$

Copyright © by SIAM. Unauthorized reproduction of this article is prohibited.

Replacing and combining with the other integral give the following set of integral equations:

$$\tau^* \hat{H}_A(T) = H_F f'(Q^*) \int_{T-\tau^*}^{T} \tilde{Q}(u)\, du, \tag{4.5}$$

$$\theta^* \hat{H}_B(T) = H_F g'(Q^*) \int_{T-\theta^*}^{T} \tilde{Q}(u)\, du. \tag{4.6}$$

Equations (4.5)–(4.6) allow us to compute the axially averaged hematocrit perturbation. To do so we require the flow perturbation and its history. The problem is closed when we linearize the constitutive relation (3.3). Using the notation developed in section 3.3 we see that

$$\begin{aligned} Q(t) &= Q^* + \left.\frac{\partial \psi}{\partial \bar{H}_A}\right|_{Q^*} \left(\bar{H}_A(t) - \bar{H}_A^*\right) + \left.\frac{\partial \psi}{\partial \bar{H}_B}\right|_{Q^*} \left(\bar{H}_B(t) - \bar{H}_B^*\right), \\ \Rightarrow \tilde{Q}(t) &= \left.\frac{\partial \psi}{\partial \bar{H}_A}\right|_{Q^*} \hat{H}_A(t) + \left.\frac{\partial \psi}{\partial \bar{H}_B}\right|_{Q^*} \hat{H}_B(t). \end{aligned}$$

The partial derivatives are straightforward to compute and are given by

$$\begin{aligned} \left.\frac{\partial \psi}{\partial \bar{H}_A}\right|_{Q^*} &= -Q^*(1-Q^*)\frac{\mu_A'^*}{\mu_A^*}, \\ \left.\frac{\partial \psi}{\partial \bar{H}_B}\right|_{Q^*} &= Q^*(1-Q^*)\frac{\mu_B'^*}{\mu_B^*}. \end{aligned}$$

Combining (4.5)–(4.6) and the expression for $\tilde{Q}(t)$ results in the linear integral equation

$$\tilde{Q}(T) = \frac{b}{\tau^*} \int_{T-\tau^*}^{T} \tilde{Q}(u)\, du + \frac{c}{\theta^*} \int_{T-\theta^*}^{T} \tilde{Q}(u)\, du, \tag{4.7}$$

where the dimensionless parameters $b$ and $c$ are the same as those defined in Theorem 3.2,

$$b = -H_F Q^*(1-Q^*) f'(Q^*) \frac{\mu_A'^*}{\mu_A^*}, \tag{4.8}$$

$$c = +H_F Q^*(1-Q^*) g'(Q^*) \frac{\mu_B'^*}{\mu_B^*}. \tag{4.9}$$

Equations (4.7)–(4.8) completely determine the linear stability of the steady state flow rate $Q^*$ to a perturbation $\tilde{Q}(T)$ such that $\tilde{Q}(T) = 0$ for all $T < 0$ and $\tilde{Q}(0) \neq 0$.

The characteristic equation can be obtained by seeking a solution of the linear integral equation in the form

$$\tilde{Q}(T) = \tilde{Q}(0) e^{\lambda T}, \tag{4.10}$$

where $\lambda$ is complex. A nontrivial solution of (4.7) subject to the solution (4.10) exists if and only if $\lambda$ satisfies the characteristic equation

$$1 = b\frac{(1-e^{-\lambda\tau})}{\lambda\tau} + c\frac{(1-e^{-\lambda\theta})}{\lambda\theta},$$

Copyright © by SIAM. Unauthorized reproduction of this article is prohibited.

where we have dropped the $*$ for convenience. It will prove more fruitful if we make a change of variables and eliminate one of the delay times in favor of the ratio of the delay times. If we redefine $\hat{\lambda} = \lambda\tau$, then we obtain

$$1 = b\frac{(1-e^{-\lambda})}{\lambda} + c\frac{(1-e^{-\lambda\gamma})}{\lambda\gamma}, \tag{4.11}$$

where again we have dropped the hats for convenience. We have introduced a new dimensionless parameter, $\gamma$, which is the ratio of the steady state delay times, i.e.,

$$\gamma = \frac{\theta}{\tau} = \frac{Q^*}{\alpha(1-Q^*)}. \tag{4.12}$$

It is clear from l'Hôpital's rule that $\lambda = 0$ is not a root of (4.11) unless $b + c = 1$. This is a degenerate case and coincides with the creation of multiple equilibria, as demonstrated in section 3.3. We will not analyze this case here but focus instead on the modified characteristic equation,

$$\lambda = b(1-e^{-\lambda}) + \frac{c}{\gamma}(1-e^{-\lambda\gamma}), \tag{4.13}$$

where we ignore the zero root of (4.13). This characteristic equation depends on the three dimensionless parameters, $b$, $c$, and $\gamma$. The delay time ratio $\gamma$ generally takes values on $(0,\infty)$ depending on the network parameters. However, we will consider only networks with values of $\gamma \in (0,1)$ since interchanging the vessel lengths and diameters results in $\alpha \to 1/\alpha$ and $Q^* \to 1-Q^*$. This implies that $\gamma \to 1/\gamma$, which recovers the original domain.

**5. The characteristic equation.** The characteristic equation (4.13) governs the stability of the two-node network. It is similar to a characteristic equation that has received some attention in the delay differential equation literature,

$$\lambda + a + be^{-\tau_1\lambda} + ce^{-\tau_2\lambda} = 0, \tag{5.1}$$

where $\tau_1$ and $\tau_2$ are the delays and $a$, $b$, and $c$ are free parameters. Clearly our characteristic equation is related, but it is not simply a special case of (5.1)—it is important that the delay $\gamma$ appear explicitly both inside and outside the exponential function in (4.13).

Several authors have considered the solutions of (5.1) using a variety of techniques [19, 9, 18, 2, 25]. The central question is whether there are any roots with $\mathrm{Re}(\lambda) > 0$. Hayes [19] studied the single delay problem ($c = 0$) and found conditions on the parameters for which all the roots lie to the left of the imaginary axis. The single delay equation is also discussed by El'sgol'ts and Norkin using the method of D-partitions [9]. In this method, the $ab$-parameter plane is divided into regions, each of which contains an integer number of roots with $\mathrm{Re}(\lambda) > 0$. The regions are separated by partition curves on which roots cross the imaginary axis. The general two delay problem was studied by Hale and Huang [18], who partitioned the $\tau_1\tau_2$-parameter plane into regions containing an integer number of roots with $\mathrm{Re}(\lambda) > 0$. Bélair and Campbell [2] considered the case with $a = 0$ and found the stability region in the $c\tau_2$-parameter plane after normalizing $b = 1$. Mahaffy, Zak, and Joiner [25] returned to the general

Copyright © by SIAM. Unauthorized reproduction of this article is prohibited.

case, after normalizing $\tau_1 = 1$, and determined instability surfaces in the *abc*-parameter space as a function of delay $\tau_2$. Our characteristic equation is easy to analyze using a similar approach; we divide the *cb*-plane into regions which contain a given number of roots, and we do this for different values of $\gamma$.

In section 5.1 we show that the roots of the characteristic equation with $\mathrm{Re}(\lambda) > 0$ (if they exist) are located within a bounded domain in the complex plane. In section 5.2 we show that if $b + c > 1$, there is exactly one positive real root, and that if $b + c < 1$, there are either two positive real roots or zero positive real roots. We also derive a parametric expression for the curve that separates the region of zero positive real roots from that of two positive real roots. In section 5.3 we derive parametric expressions for the Hopf bifurcation curves in the *cb*-plane on which the roots are purely imaginary, and we prove that $bc < 0$ is a necessary condition for the existence of purely imaginary roots. By combining the real root case and the imaginary root case we are therefore able to build a complete picture of the distribution of roots in the *cb*-plane as we vary the value of $\gamma \in (0, 1)$.

**5.1. Complex roots.** The most general solution of the characteristic equation (4.13) is complex and takes the form

$$\lambda = \sigma + i\omega, \tag{5.2}$$

where $\sigma$ is the real part and $\omega$ is the imaginary part. Substituting into the characteristic equation and separating real and imaginary terms lead to the set of equations

$$\sigma - b\left(1 - e^{-\sigma}\cos(\omega)\right) - \frac{c}{\gamma}\left(1 - e^{-\sigma\gamma}\cos(\omega\gamma)\right) = 0, \tag{5.3}$$

$$\omega - be^{-\sigma}\sin(\omega) - \frac{c}{\gamma}e^{-\sigma\gamma}\sin(\omega\gamma) = 0, \tag{5.4}$$

which must be satisfied simultaneously. The following theorem is proved below.

Theorem 5.1.

1. *Assume that* $b < 0$ *and* $c < 0$. *Then there are no roots with* $\sigma > 0$.
2. *Assume that* $b > 0$ *and* $c < 0$. *If a root with* $\sigma > 0$ *exists, then it is located within a bounded region, namely,* $(\sigma, \omega) \in (0, 2b) \times [-(b + |c|/\gamma), b + |c|/\gamma]$.
3. *Assume that* $b < 0$ *and* $c > 0$. *If a root with* $\sigma > 0$ *exists, then it is located within a bounded region, namely,* $(\sigma, \omega) \in (0, 2c/\gamma) \times [-(|b| + c/\gamma), |b| + c/\gamma]$.
4. *Assume that* $b > 0$ *and* $c > 0$. *If a root with* $\sigma > 0$ *exists, then it is located within a bounded region, namely,* $(\sigma, \omega) \in (0, 2b + 2c/\gamma) \times [-(b + c/\gamma), b + c/\gamma]$.

*Proof.* Assume that there is a root with $\sigma > 0$. Then the following inequalities are true:

$$0 < 1 - e^{-\sigma}\cos(\omega) < 2, \tag{5.5}$$

$$0 < 1 - e^{-\sigma\gamma}\cos(\omega\gamma) < 2, \tag{5.6}$$

$$-1 < e^{-\sigma}\sin(\omega) < 1, \tag{5.7}$$

$$-1 < e^{-\sigma\gamma}\sin(\omega\gamma) < 1. \tag{5.8}$$

First consider the case of $b < 0$ and $c < 0$. The inequalities and equation (5.3) imply that $\sigma < 0$, which is a contradiction. Thus there are no roots with $\sigma > 0$ when $b < 0$ and $c < 0$.

Copyright © by SIAM. Unauthorized reproduction of this article is prohibited.

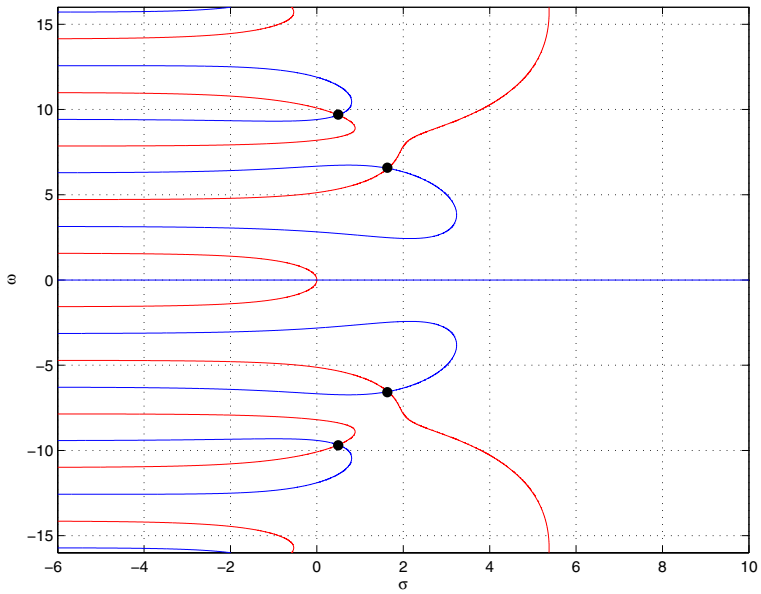


**Figure 7.** *The zero contours of $R(\sigma,\omega)$ and $I(\sigma,\omega)$ are shown in red and blue, respectively. The intersection points are solutions of (5.3)–(5.4). For $b=-8$, $c=2$, and $\gamma=0.2$ there are two complex conjugate roots with $\sigma>0$.*

Consider now the case of $b>0$ and $c<0$. The inequalities and equations (5.3) and (5.4) imply that

$$\sigma < 2b, \tag{5.9}$$

$$|\omega| \le b + \frac{|c|}{\gamma}, \tag{5.10}$$

which shows that if a root with $\sigma>0$ exists, then it is located within a bounded region in the complex plane. A similar argument can be made for the case of $b<0$ and $c>0$ and for the case of $b>0$ and $c>0$. ■

The solutions to the characteristic equation (4.13) may be visualized as follows. For a given set of parameters $b$, $c$, and $\gamma$, the left-hand sides of (5.3) and (5.4) are functions of $\sigma$ and $\omega$, and we will denote these functions as $R(\sigma,\omega)$ and $I(\sigma,\omega)$. The intersection of the zero contours of both functions will be the roots of the characteristic equation. An example is shown in Figure 7 for the values of $b=-8$, $c=2$, and $\gamma=0.2$. The roots of the characteristic equation are clearly marked, and in this case there are two pairs of complex conjugate roots with $\sigma>0$. The root at $(0,0)$ is not a solution of (4.11) since $b+c\neq 1$.

**5.2. Real roots.** We will search for real roots by looking for a solution of the form $\lambda=\sigma+i0$, which leads to the simplified characteristic equation

$$\sigma - b(1-e^{-\sigma}) - \frac{c}{\gamma}\left(1-e^{-\sigma\gamma}\right) = 0. \tag{5.11}$$

The following theorem is proved below.

Copyright © by SIAM. Unauthorized reproduction of this article is prohibited.

Theorem 5.2.

1. *If $b + c > 1$ there is exactly one positive real root.*
2. *If $b + c < 1$ there are either two positive real roots or none at all.*
   (a) *The boundary that separates the regions of zero positive real roots from two positive real roots is defined parametrically by*

$$\det = -\frac{1}{\gamma}e^{-\sigma} + e^{-\sigma\gamma} + \frac{(1-\gamma)}{\gamma}e^{-\sigma(1+\gamma)}, \tag{5.12}$$

$$b(\sigma) = \frac{1}{\det}\left(\sigma e^{-\sigma\gamma} + \frac{e^{-\sigma\gamma}-1}{\gamma}\right), \tag{5.13}$$

$$c(\sigma) = \frac{1}{\det}\left(-\sigma e^{-\sigma} + (1-e^{-\sigma})\right), \tag{5.14}$$

   *where $\sigma \in [0, \infty)$. This parametric curve requires $bc < 0$ and lies in the fourth quadrant (for $0 < \gamma < 1$).*
   (b) *The boundary that separates the regions of two positive real roots from one positive real root is defined by the line segment $b + c = 1$, with $b < -\gamma/(1-\gamma)$ and $c > 1/(1-\gamma)$.*

*Proof.* The proof of these results is straightforward and is accomplished mostly by curve sketching. Roots of the characteristic equation (5.11) are given by roots of the function $F(\sigma)$,

$$F(\sigma) = \sigma - b(1-e^{-\sigma}) - \frac{c}{\gamma}\left(1-e^{-\sigma\gamma}\right). \tag{5.15}$$

The function $F(\sigma)$ is continuous and has the following properties:

$$\begin{aligned} F(0) &= 0, \\ \lim_{\sigma\to+\infty} F(\sigma) &= +\infty, \\ \lim_{\sigma\to-\infty} F(\sigma) &= \operatorname{sign}(b)\,\infty, \\ F'(0) &= 1-(b+c). \end{aligned}$$

In each region of the $cb$-plane we can sketch the function $F(\sigma)$ and determine the number of roots. This is simple in the first, second, and third quadrants and confirms the theorem in these regions. It is also unambiguous in the fourth quadrant with $b + c > 1$. However, in the fourth quadrant with $b + c < 1$ the curves are ambiguous and it is helpful to reconsider the original characteristic equation and write it in the form

$$-\sigma + b + \frac{c}{\gamma} = be^{-\sigma} + \frac{c}{\gamma}e^{-\sigma\gamma}. \tag{5.16}$$

The function on the left, which we denote as $L(\sigma)$, represents a straight line of slope $-1$ and intersects $b + c/\gamma$. The function on the right, which we denote as $R(\sigma)$, represents a linear combination of two different exponentials. We see that it has the same intersection at $\sigma = 0$, and that $R'(0) = -(b+c)$. As $\sigma \to \infty$ we see that $R \to 0$ from above if $c > 0$ and from below if $c < 0$ (remember that $\gamma < 1$). In addition, there exists one value of $\sigma$ where $R = 0$ if and only if $-\frac{\gamma b}{c} > 1$. Finally, there exists one value of $\sigma$ where $R' = 0$ if and only if $-\frac{b}{c} > 1$.

Copyright © by SIAM. Unauthorized reproduction of this article is prohibited.

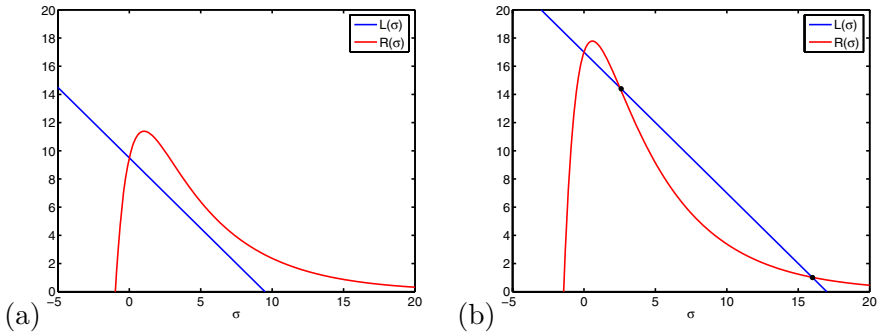


**Figure 8.** *The functions $L$ and $R$ are shown in blue and red, respectively, at two points in the fourth quadrant with $b + c \leq 1$ and $\gamma = 0.2$. (a) There are no nonzero intersections of $L$ and $R$ for $c = 3.5$ and $b = -8$. (b) There are two nonzero intersections of $L$ and $R$ for $c = 5$ and $b = -8$.*

In the fourth quadrant with $b+c < 1$ the function $R(\sigma)$ may never intersect the line $L(\sigma)$ or it may intersect it twice. Typical curves are shown in Figure 8. In Figure 8a we plot $L$ and $R$ as functions of $\sigma$ in blue and red, respectively, for $b = -8$, $c = 3.5$, and $\gamma = 0.2$. Notice that there are no nonzero intersections in this case (the intersection at $\sigma = 0$ is not a root of (4.11) since $b + c \neq 1$). Increasing the value of $c$ to $c = 5$ leads to two nonzero intersections, as shown in Figure 8b. The transition from zero to two roots takes place when the two curves are tangent; this occurs when both the functions and their derivatives are equal:

$$b(1 - e^{-\sigma}) + c\frac{(1 - e^{-\sigma\gamma})}{\gamma} = \sigma, \tag{5.17}$$

$$be^{-\sigma} + ce^{-\sigma\gamma} = 1. \tag{5.18}$$

This represents two linear equations in $b$ and $c$ which can be solved to give

$$\det = -\frac{1}{\gamma}e^{-\sigma} + e^{-\sigma\gamma} + \frac{(1-\gamma)}{\gamma}e^{-\sigma(1+\gamma)}, \tag{5.19}$$

$$b(\sigma) = \frac{1}{\det}\left(\sigma e^{-\sigma\gamma} + \frac{e^{-\sigma\gamma} - 1}{\gamma}\right), \tag{5.20}$$

$$c(\sigma) = \frac{1}{\det}\left(-\sigma e^{-\sigma} + (1 - e^{-\sigma})\right). \tag{5.21}$$

Since we are searching for nonnegative roots we can assume that $\sigma \in [0, \infty)$ and these equations therefore define a parametric curve in the $cb$-plane. In addition, applying l'Hôpital's rule demonstrates that

$$\lim_{\sigma\to 0^+} b(\sigma) = \frac{-\gamma}{1-\gamma}, \tag{5.22}$$

$$\lim_{\sigma\to 0^+} c(\sigma) = \frac{1}{1-\gamma}, \tag{5.23}$$

which is the point of intersection of the lines $b + c = 1$ and $b = -\gamma c$ and is in the fourth quadrant for $0 < \gamma < 1$. Moreover, it is true that $\lim_{\sigma\to\infty} b(\sigma) = -\infty$ and $\lim_{\sigma\to\infty} c(\sigma) = \infty$

Copyright © by SIAM. Unauthorized reproduction of this article is prohibited.

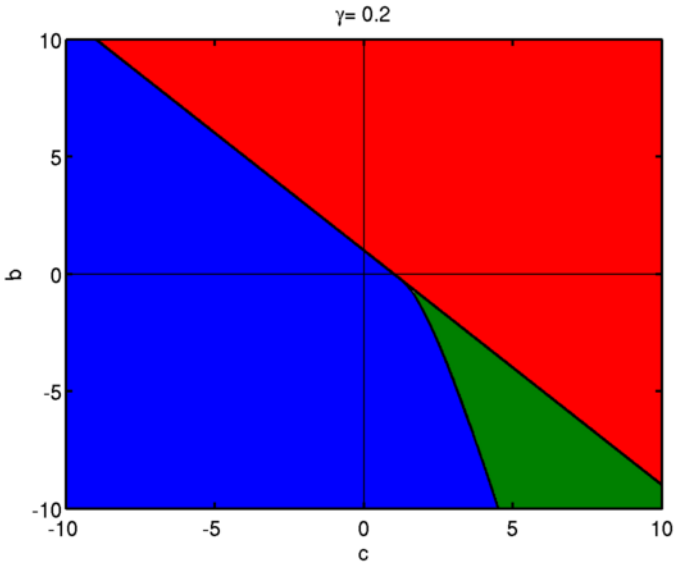


**Figure 9.** *The cb-plane is partitioned into three regions. In the blue region there are no real positive roots. In the red region there is one real positive root. In the green region there are two real positive roots.*

and that neither $b$ nor $c$ can ever become zero. The parametric curve is therefore located in the fourth quadrant. ■

In Figure 9 we plot the $cb$-plane for $\gamma = 0.2$ as an example. The regions containing zero, one, or two positive real roots are clearly marked. Let us define the $b+c=1$ line to be $\gamma_1$ and the parametric curve that separates the region of zero positive real roots from two positive real roots to be $\gamma_2$. For this value of $\gamma$, the point of intersection of $\gamma_1$ and $\gamma_2$ is $(5/4, -1/4)$.

**5.3. Imaginary roots.** We search for imaginary roots by looking for solutions of the characteristic equation of the form $\lambda = 2i\omega$. This particular choice leads to convenient algebra, and the characteristic equation decomposes into

$$\omega = b\cos(\omega)\sin(\omega) + \frac{c}{\gamma}\cos(\omega\gamma)\sin(\omega\gamma), \tag{5.24}$$

$$0 = -b\sin^2(\omega) - \frac{c}{\gamma}\sin^2(\omega\gamma). \tag{5.25}$$

We prove the following theorem below.

Theorem 5.3. *For any given value of $\gamma \in (0,1)$ there are an infinite number of Hopf bifurcation curves in the cb-plane on which there exists a purely imaginary root. These bifurcation curves are denumerable and we will label them as $\Gamma_j$ for $j = 0, 1, 2, \ldots$. Each bifurcation curve is defined on a finite, closed interval of the form $[\omega_j, \omega_{j+1}]$. The curve $\Gamma_j$ is defined parametrically by*

$$b(\omega) = \frac{-\omega\sin(\omega\gamma)}{\sin(\omega)\sin(\omega(1-\gamma))}, \tag{5.26}$$

$$c(\omega) = \frac{\omega\gamma\sin(\omega)}{\sin(\omega\gamma)\sin(\omega(1-\gamma))} \tag{5.27}$$

Copyright © by SIAM. Unauthorized reproduction of this article is prohibited.

*for $\omega \in [\omega_j, \omega_{j+1}]$ and is located in either the second or fourth quadrant. The endpoints $\omega_j$ and $\omega_{j+1}$ are found by sorting the roots of* $\sin(\omega)$, $\sin(\omega\gamma)$, *and* $\sin(\omega(1-\gamma))$ *into ascending order and choosing the $j$th and $(j+1)$th roots, respectively. The Hopf bifurcation curve $\Gamma_0$ is defined on $[0, \pi]$, is semi-infinite, and originates from $(-\gamma/(1-\gamma), 1/(1-\gamma))$. All other bifurcation curves are infinite.*

*Proof.* Equations (5.24)–(5.25) define a linear system of equations in $b$ and $c$ which can be solved to give (5.26)–(5.27). These are parametric equations in $\omega$ with $bc < 0$. There is a new branch whenever one or more of the terms $\sin(\omega)$, $\sin(\omega\gamma)$, or $\sin(\omega(1-\gamma))$ is zero. The roots of these functions are $k\pi$, $l\pi/\gamma$, and $m\pi/(1-\gamma)$, respectively, for integers $k$, $l$, and $m$. Since we are considering $\gamma < 1$ the first two roots are $\omega_0 = 0$ and $\omega_1 = \pi$. The bifurcation curve $\Gamma_0$ is therefore defined for $\omega \in [0, \pi]$. It is semi-infinite since

$$\lim_{\omega \to 0^+} b(\omega) = \frac{-\gamma}{1-\gamma}, \tag{5.28}$$

$$\lim_{\omega \to 0^+} c(\omega) = \frac{1}{1-\gamma}, \tag{5.29}$$

$$\lim_{\omega \to \pi^-} b(\omega) = -\infty, \tag{5.30}$$

$$\lim_{\omega \to \pi^-} c(\omega) = 0^+ \tag{5.31}$$

and can be viewed as a continuation of the real root curve $\gamma_2$. All other bifurcation curves are infinite because of the linear dependence on $\omega$ in (5.26)–(5.27), even if there exist $\omega$ values where all three functions are simultaneously zero. Since $bc < 0$ every bifurcation curve is located in either the second or fourth quadrant. ∎

In Figure 10 we plot the first few Hopf bifurcation curves in the $cb$-plane for $\gamma = 0.2$ as an example. As expected from section 5.1, all of the Hopf bifurcation curves $\Gamma_j$ lie in the second and fourth quadrants where $bc < 0$. The first Hopf bifurcation curve, $\Gamma_0$, always lies in the fourth quadrant since $\gamma < 1$. The Hopf bifurcation curves $\Gamma_j$ and the real root curves $\gamma_1$ and $\gamma_2$ separate the $cb$-plane into distinct regions with different numbers of roots with positive real part. Changing the value of $\gamma$ changes the location of the curves $\Gamma_j$ and $\gamma_2$. For small $\gamma$ the curves start relatively close to the origin, while as $\gamma \to 1$ the curves move off to infinity. It is clear graphically that on every curve there exists a unique point which is closest to the origin. In addition, it is also clear that the point closest to the origin lies on the first bifurcation curve $\Gamma_0$, but we have been unable to prove either of these results analytically. The next section will demonstrate that this conjecture has important implications for the onset of instability.

**6. The onset of instability.** The linear stability of the equilibrium solution to microvascular blood flow in a two-node network is governed by the characteristic equation (4.13). In the previous section we built a complete picture of the distribution of roots in the $cb$-plane for different values of $\gamma$. In particular, we found parametric equations for curves in the $cb$-plane that separated regions with different numbers of roots with positive real part—equations (5.26)–(5.27). The question of stability of a given equilibrium state of the microvascular blood flow model can now be answered as follows. Choose a set of network parameters. We can use (3.8) to compute the equilibrium flow ratio $Q^*$. If we recall from section 4 the definitions of

Copyright © by SIAM. Unauthorized reproduction of this article is prohibited.

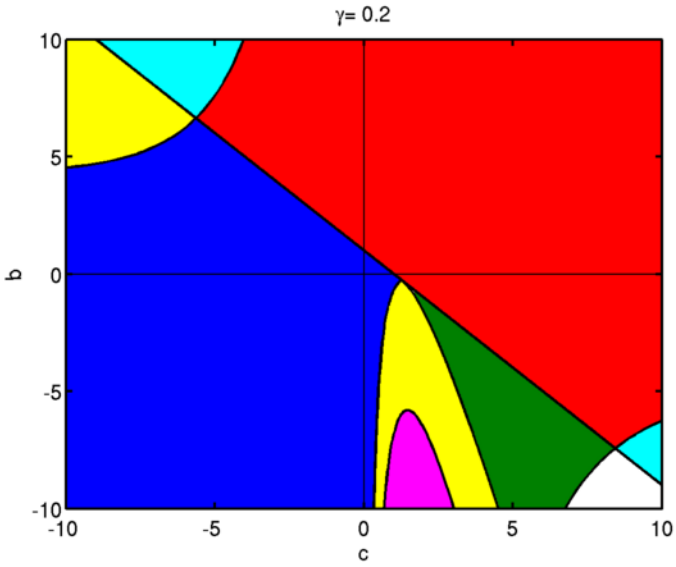


**Figure 10.** *The cb-plane is partitioned into distinct regions with different numbers of real and complex roots. In the blue region there are no real positive or complex roots with positive real part. In the red region there is one real positive root. In the green region there are two real positive roots. In the yellow region there is one pair of complex conjugate roots. In the magenta region there are two pairs of complex conjugate roots. In the cyan region there is one real positive root and a pair of complex conjugate roots. In the white region there are two real positive roots and a pair of complex conjugate roots.*

$b$, $c$, and $\gamma$,

$$b = -H_F Q^*(1-Q^*)f'(Q^*)\frac{\mu_A'^*}{\mu_A^*},$$
$$c = +H_F Q^*(1-Q^*)g'(Q^*)\frac{\mu_B'^*}{\mu_B^*},$$
$$\gamma = \frac{Q^*}{\alpha(1-Q^*)},$$

then each set of network parameters will map to a point in the $cb$-plane defined by $\gamma$. The system is stable or unstable depending on the location of the point.

The shortcomings of this approach are obvious; every point in network parameter space potentially maps to a different point in a different $cb$-plane defined by a different value of $\gamma$. While it is possible to use this approach to test the stability of a given network, this is all but useless as a tool for finding unstable parameter values. If, however, we focus our attention on the parametric models of (2.6) and (2.7), then $b$ and $c$ simplify to

$$b = -\delta H_F Q^*(1-Q^*)f'(Q^*), \tag{6.1}$$
$$c = +\delta H_F Q^*(1-Q^*)g'(Q^*). \tag{6.2}$$

As in the section on equilibrium solutions, only four network parameters are required in order to determine $Q^*$. These parameters are the length ratio $l_A/l_B$, the diameter ratio $d_B/d_A$, the combined Fåhræus–Lindqvist parameter $\delta H_F$, and the plasma skimming parameter $p$.

Copyright © by SIAM. Unauthorized reproduction of this article is prohibited.

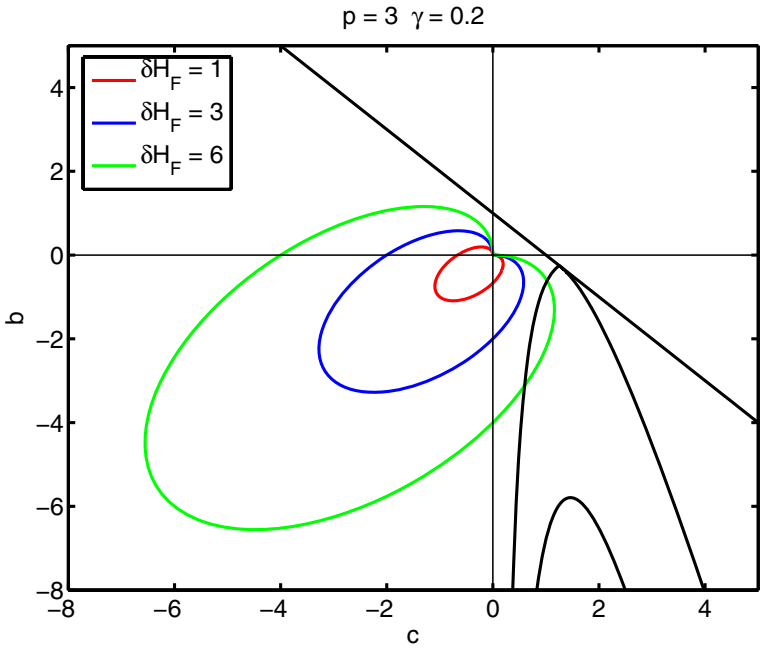


**Figure 11.** *The partitioned cb-plane in Figure 10 is shown with the colors removed and the scale changed for clarity. In addition, the parametric curve defined by (6.1)–(6.2) is shown for three different values of $\delta H_F$. In each case the curve is parameterized by $Q^* \in [0,1]$, launches from the origin, moves in a counter-clockwise direction, and ends at the origin. For $\delta H_F = 1$ (red curve) and $\delta H_F = 3$ (blue curve) the curve always remains in the stable region, while for $\delta H_F = 6$ (green curve) the curve crosses the first bifurcation curve $\Gamma_1$.*

In section 6.1 we show that it is possible to map the bifurcation curves to the $(Q^*, \delta H_F)$-plane for a fixed value of $\gamma$ and $p$. In section 6.2 we consider the impact of changing $\gamma$, while in section 6.3 we show that the bifurcation curves can be mapped to a variety of network parameter planes. Finally, in section 6.4 we investigate the dependence on $p$, and we confirm our predictions by direct numerical simulation in section 6.5.

**6.1. The $(Q^*, \delta H_F)$-plane.** As a good example, let us choose $p = 3$ and $\gamma = 0.2$ and hold these values fixed. Then (6.1)–(6.2) define a parametric curve in the $cb$-plane parameterized by $Q^*$. The shape and size of this curve is influenced by the plasma skimming parameter $p$ (via $f'$ and $g'$) and the combined parameter $\delta H_F$. For given values of $\delta H_F$ and $p$, this curve is continuous and closed and has clockwise orientation for $Q^* \in [0,1]$.

In Figure 11 we show parametric curves in the $cb$-plane with $\gamma = 0.2$ and $p = 3$ for $\delta H_F = 1, 3, 6$. In each case, the curve originates from the origin at $Q^* = 0$, intersects the $c = 0$ axis where $g' = 0$, intersects the $b = 0$ axis where $f' = 0$, and returns to the origin as $Q^* \to 1$. Increasing $\delta H_F$ results in larger parametric curves with the same basic shape since $\delta H_F$ is simply a linear scale factor in (6.1)–(6.2). Notice, however, that for $\delta H_F = 1$ and $\delta H_F = 3$, the curve remains in the stable region while for $\delta H_F = 6$ the curve passes into the unstable region. There must therefore be a minimum value of $\delta H_F$ below which the system is stable. For $\delta H_F$ slightly larger than this minimum value, there are Hopf bifurcations at the two locations where the parametric curve crosses the first Hopf bifurcation curve. Increasing

Copyright © by SIAM. Unauthorized reproduction of this article is prohibited.

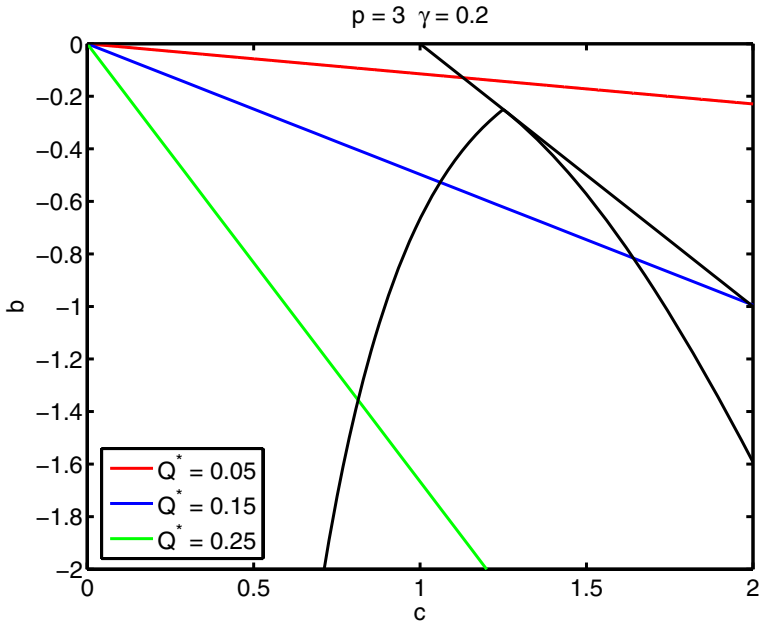


**Figure 12.** *The partitioned cb-plane in Figure 10 is shown with the colors removed and the scale changed for clarity. In addition, the parametric ray defined by (6.1)–(6.2) is shown for three different values of $Q^*$. In each case the ray is parameterized by $\delta H_F \in [0, \infty)$ and launches from the origin. For $Q^* = 0.05$ (red ray) the ray crosses into the single real root region for large enough $\delta H_F$ but never enters a region with a complex root. For $Q^* = 0.15$ (blue ray) and $Q^* = 0.25$ (green ray) the ray crosses the first bifurcation curve $\Gamma_1$ for large enough $\delta H_F$.*

$\delta H_F$ would result in the parametric curve crossing into the one real root and two real roots regions, respectively. For very large $\delta H_F$ it is possible for the parametric curve to cross other Hopf bifurcation curves.

It is possible to map the real root curves $\gamma_1$ and $\gamma_2$ and the Hopf bifurcation curves into the $(Q^*, \delta H_F)$-plane using an alternative interpretation of (6.1)–(6.2). If we choose a value of $Q^*$ and let $\delta H_F$ vary from 0 to $\infty$, then the parametric curve is simply a parametric ray with slope

$$\frac{b}{c} = -\frac{f'(Q^*)}{g'(Q^*)}.$$

In Figure 12 we plot three different rays for $p = 3$ and $\gamma = 0.2$. For small $Q^*$ there is an intersection with $\gamma_1$, but there may be no intersection with either $\gamma_2$ or $\Gamma_0$. For $Q^*$ larger than some critical value, however, the parametric ray first intersects $\Gamma_0$, then intersects $\gamma_2$, and then intersects $\gamma_1$. This pattern continues as we increase $Q^*$ until the parametric ray no longer intersects $\gamma_1$. For even larger $Q^*$ the ray no longer intersects $\gamma_2$, but it continues to intersect $\Gamma_0$ as $Q^* \to Q_g$. Any ray may also intersect a higher order Hopf bifurcation curve, but this occurs for much larger values of $\delta H_F$ since these curves are located farther away from the origin.

The value of $\delta H_F$ at which any parametric ray crosses $\gamma_1$ may be computed as follows. Recall from section 5.2 that $\gamma_1$ is defined by $b + c = 1$. Using the definition of $b$ and $c$ in

Copyright © by SIAM. Unauthorized reproduction of this article is prohibited.

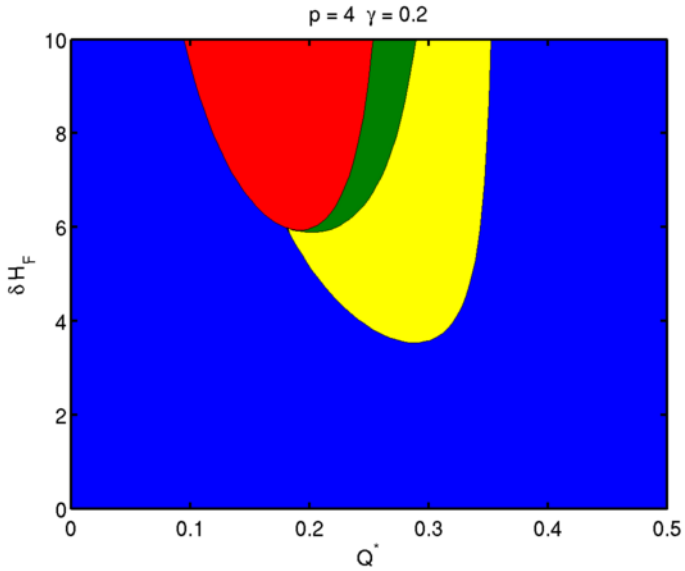


**Figure 13.** *The bifurcation curves and associated regions in the cb-plane are mapped to the $(Q^*, \delta H_F)$-plane. The boundaries between the regions are computed by determining, for a given value of $Q^*$, the value of $\delta H_F$ for which the ray crosses the boundary curves of Figure 10. In the blue region there are no complex roots with positive real part. In the yellow region there is one pair of complex conjugate roots with positive real part. In the red region there is one positive real root, and in the green region there are two positive real roots.*

(6.1)–(6.2) we can solve for $\delta H_F$:

$$\delta H_F = \frac{1}{Q^*(1-Q^*)(g'(Q^*) - f'(Q^*))}.$$

In Figure 13 we plot $\gamma_1$ in the $(Q^*, \delta H_F)$-plane for $p = 4$ and $\gamma = 0.2$. For small $Q^*$ the value of $\delta H_F$ is very large. As $Q^*$ increases, the value of $\delta H_F$ decreases and then increases, reaching an asymptote at the value of $Q^*$ where $g'(Q^*) - f'(Q^*) = 0$.

The value of $\delta H_F$ at which any parametric ray crosses $\Gamma_0$ may be computed by using the definition of the Hopf bifurcation curves, equations (5.26)–(5.27). A ray from the origin to a point on any Hopf bifurcation curve has slope

$$\frac{b}{c} = -\frac{\sin^2(\omega^*\gamma)}{\gamma \sin^2(\omega^*)}.$$

Recall from section 5.3 that the first Hopf bifurcation curve, $\Gamma_0$, is defined for $\omega \in [0, \pi]$. For a given value of $Q^*$ we can compute the value of $\omega^* \in [0, \pi]$ which results in identical slopes. The coordinates of a Hopf bifurcation point on $\Gamma_0$ can then be computed by solving

$$\frac{-\omega^* \sin(\omega^*\gamma)}{\sin(\omega^*)\sin(\omega^*(1-\gamma))} = -\delta H_F f'(Q^*)Q^*(1-Q^*)$$

for $\delta H_F$. A similar calculation can be made in order to map $\gamma_2$ onto the $(Q^*, \delta H_F)$-plane. In Figure 13 we also plot $\gamma_2$ and $\Gamma_0$ in the $(Q^*, \delta H_F)$-plane for $p = 4$ and $\gamma = 0.2$. Notice

Copyright © by SIAM. Unauthorized reproduction of this article is prohibited.

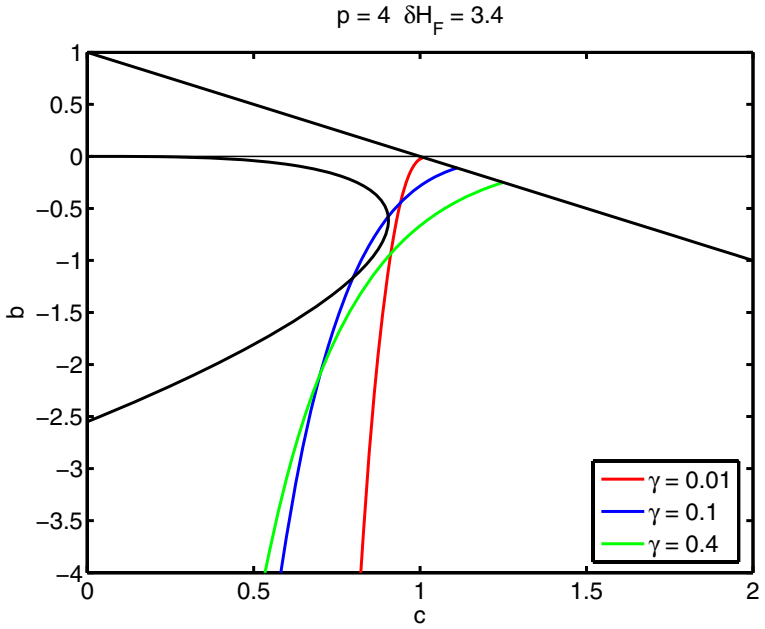


**Figure 14.** *The first Hopf bifurcation curve $\Gamma_0$ is shown for different values of $\gamma$. The line $b + c = 1$ is shown (in black) as well as the parametric curve for $p = 4$ and $\delta H_F = 3.4$ (also in black). For very small $\gamma$ (red), the bifurcation curve $\Gamma_0$ starts close to $(1, 0)$ but never crosses the parametric curve. For an intermediate value of $\gamma$ (blue), $\Gamma_0$ crosses the parametric curve twice. For a larger value of $\gamma$ (green), $\Gamma_0$ starts too far from the origin to be able to cross the parametric curve.*

that there is a critical value of $Q^*$ which results in a minimum value of $\delta H_F$ below which the system is stable. As we increase $\delta H_F$ above this minimum value, there exists an interval of $Q^*$ for which the system is unstable.

**6.2. Changing $\gamma$.** We have so far focused our attention on an arbitrary value of $\gamma$ for the sake of clarity. As indicated in section 5.3, changing $\gamma$ results in the Hopf bifurcation curves moving in the $cb$-plane. In Figure 14 we show a fixed parametric curve with $p = 4$ and $\delta H_F = 3.4$ in the presence of Hopf bifurcation curves for several different values of $\gamma$. We plot only the first Hopf bifurcation curve $\Gamma_0$ for clarity. For $\gamma = 0.01$ the Hopf bifurcation curve begins close to $(1, 0)$, and $b$ decreases so rapidly that it does not intersect the parametric curve. As $\gamma$ increases, the Hopf bifurcation curve begins further from the origin, but $b$ decreases less rapidly. Intersections are therefore possible, which is precisely the case when $\gamma = 0.1$. For larger $\gamma$, $b$ decreases less rapidly still, but the Hopf bifurcation curve begins so far from the origin that intersections are impossible as shown for $\gamma = 0.4$. There are no further intersections for increasing $\gamma$.

As indicated earlier, there is a minimum value of $\delta H_F$ at which we cross the first Hopf bifurcation curve $\Gamma_0$. This minimum value $\delta H_F^{min}$ depends on the value of $\gamma$. By repeating our previous calculation, we can extract $\delta H_F^{min}$ for each value of $\gamma$. In Figure 15 we show the results of this computation for $p = 4$. For very small $\gamma$ the minimum value of $\delta H_F$ is very large. As $\gamma$ increases, the minimum value decreases to a global minimum and then increases

Copyright © by SIAM. Unauthorized reproduction of this article is prohibited.

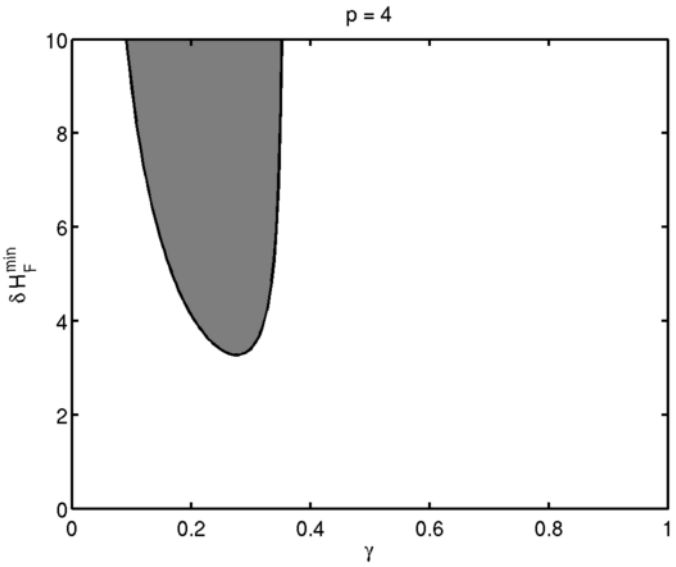


**Figure 15.** *The minimum value of $\delta H_F$ is shown versus $\gamma$ for $p = 4$. In the gray region the parametric curve defined by (6.1)–(6.2) is guaranteed to cross the first Hopf bifurcation curve $\Gamma_0$. In the white region there are no such crossings and the system is stable.*

again. We will denote this minimum value as $\delta H_F^c$, the critical value of $\delta H_F$ below which the system is stable for any value of $\gamma$. For $p = 4$ the value of $\delta H_F^c = 3.2709$. The system is guaranteed to be stable if $\delta H_F$ is less than this value. On the contrary, there exists an unstable set of parameters if $\delta H_F$ is larger than this critical value.

**6.3. Network parameter planes.** Let us now choose a value of $\delta H_F$ greater than the critical value, say, $\delta H_F = 3.4$. In Figure 16 we plot the region of instability in the $(\gamma, Q^*)$-plane by drawing a Hopf bifurcation contour at $\delta H_F = 3.4$ for $p = 4$. This contour is a simple closed curve for the following reason. Figure 15 shows that there is an interval of $\gamma$ for which the system is unstable. In addition, Figure 13 shows that for a given value of $\gamma$ there is an interval of $Q^*$ for which the system is unstable. Combining both of these findings implies that the Hopf bifurcation curve $\Gamma_0$ is a simple closed curve in the $(\gamma, Q^*)$-plane. As we increase $\delta H_F$, the simple closed curve grows and evolves.

Every point on the Hopf bifurcation curve in Figure 16 has coordinates $(\gamma, Q^*)$. Since $p = 4$ and $\delta H_F = 3.4$, there are only two network parameters undetermined—the length ratio $l_A/l_B$ and the diameter ratio $d_B/d_A$. However, we have two equations—the definition of the steady state $Q^*$, (3.8), and the definition of $\gamma$, (4.12). Using these equations we can solve for unique values of the length and diameter ratios for every point on the Hopf bifurcation curve $\Gamma_0$. The result is a simple closed curve in the $(l_A/l_B, d_B/d_A)$-plane as shown in Figure 17. The Hopf bifurcation curve emerges at approximately $(16.5, 1.8)$ as $\delta H_F$ exceeds the critical value of 3.2709. Notice that the instability region is quite narrow for $\delta H_F$ close to the critical value; as $\delta H_F$ increases, the size of the unstable region also increases.

Copyright © by SIAM. Unauthorized reproduction of this article is prohibited.

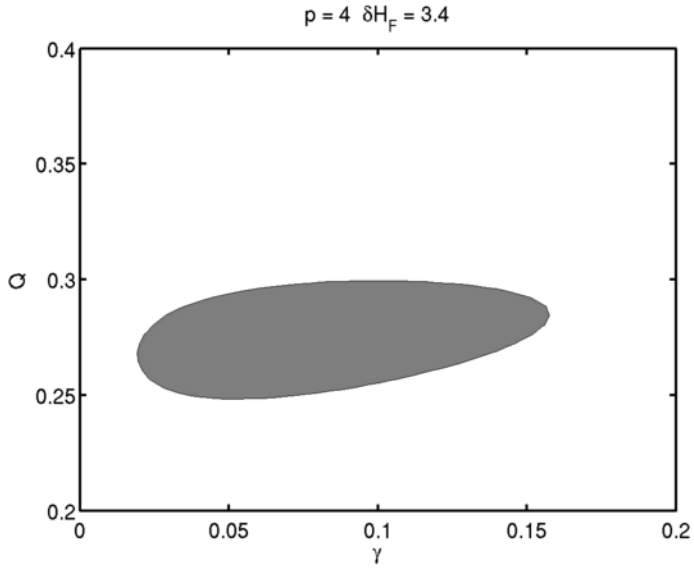


**Figure 16.** *The first Hopf bifurcation curve maps to a closed curve in the* $(\gamma, Q^*)$*-plane for* $p = 4$*,* $\delta H_F = 3.4$*. In the gray region the system is unstable to a Hopf bifurcation. In the white region it is stable. For larger values of* $\delta H_F$ *the gray region moves and expands.*

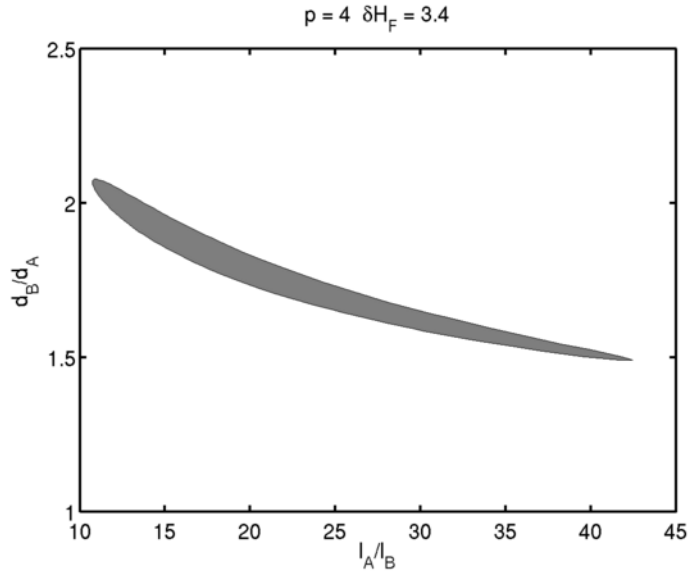


**Figure 17.** *The first Hopf bifurcation curve also maps to a closed curve in the* $(l_A/l_B, d_b/d_A)$*-plane for* $p = 4$*,* $\delta H_F = 3.4$*. The system is unstable to a Hopf bifurcation in the gray region and is stable otherwise. As* $\delta H_F$ *increases the unstable region moves and expands.*

**6.4. Changing $p$.** The discussion so far has focused on determining unstable network parameters for a single value of $p$. If we change the value of $p$ we change the shape of the parametric curves. In Figure 18 we show the parametric curves in the $cb$-plane ($\gamma = 0.2$) with

Copyright © by SIAM. Unauthorized reproduction of this article is prohibited.

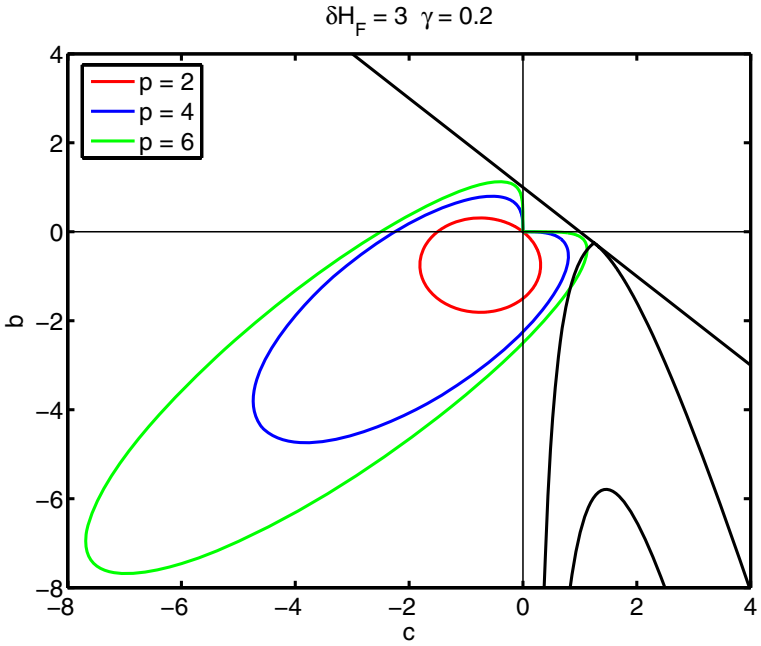


**Figure 18.** *The cb-plane with the bifurcation curves and three different parametric curves is shown for $\gamma = 0.2$, $\delta H_F = 3$. The parametric curve grows as $p$ is increased until for a sufficiently large value it crosses into the unstable region (green).*

$\delta H_F = 3$ for $p = 2, 4, 6$. Notice again that as $p$ increases the curve grows in size. For $p = 2$ and $p = 4$ it remains in the stable region, while for $p = 6$ the curve crosses the Hopf bifurcation curve $\Gamma_0$.

All of the previous computations can be repeated for any value of $p$. In particular, for every value of $p$ there is a critical value of $\delta H_F$ below which the system is stable. In Figure 19 we plot the critical value of $\delta H_F$ as a function of $p$. This curve separates a region of stability from a region of instability. It is important to note that a point in the unstable region will have associated with it a region of instability in the $(\gamma, Q^*)$-plane and a corresponding region of instability in the $(l_A/l_B, d_B/d_A)$-plane. Close to the instability boundary the regions of instability are quite small, as shown previously in Figures 16 and 17. As we move further into the unstable domain, the instability regions grow and the other Hopf bifurcation curves and the real root curves $\gamma_1$ and $\gamma_2$ can come into play. We have not explored the regions far from the instability boundary for reasons that will become clear in section 7.

**6.5. Numerical confirmation.** We have confirmed these predictions by direct numerical simulation of the governing equations (3.1)–(3.2), along with the constitutive relations (3.3)–(3.5) and boundary conditions (3.6)–(3.7). We have used a variety of algorithms, including the upwinding convection scheme and the second-order Lax–Wendroff method [1]. While the accuracy of the schemes depends on the choice of space- and time-step, all of the schemes used have agreed with the theoretical predictions on instability. This, along with previous studies [21, 4, 5], makes it clear that the fluctuations are not a result of numerical instability.

Copyright © by SIAM. Unauthorized reproduction of this article is prohibited.

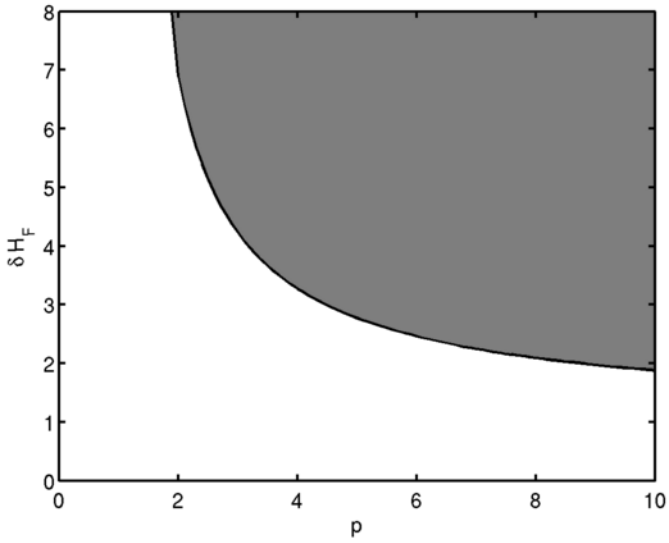


**Figure 19.** *For every value of $p$ there exists a critical value of $\delta H_F$ below which the system is stable. For values of $\delta H_F$ greater than this critical value (gray region), there exists a domain in parameter space (similar to Figures 16 and 17) for which the system is unstable. This unstable domain grows in size as you move further into the gray region.*

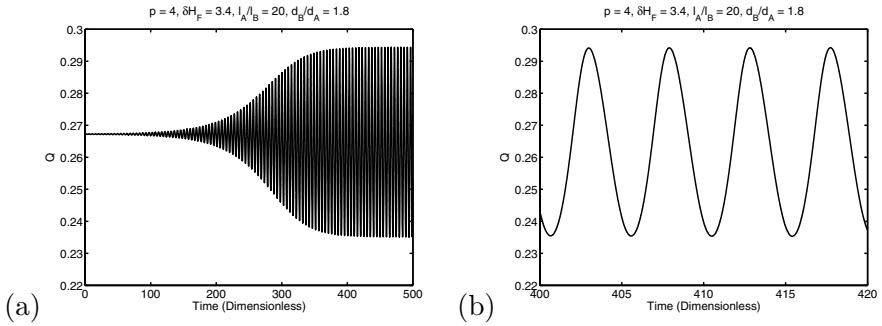


**Figure 20.** *Direct numerical simulation of (3.1)–(3.2). The system is initiated close to steady state and parameter values are chosen in the unstable domain.* (a) *The flow $Q(t)$ as a function of time demonstrating instability to a Hopf bifurcation with a growth rate close to that predicted by analysis.* (b) *A close-up of the oscillation showing that the period matches that predicted by analysis.*

In Figure 20a we plot the flow as a function of time. We used the following parameter values: $l_A/l_B = 20$, $d_B/d_A = 1.8$, $p = 4$, and $\delta H_F = 3.4$. At these parameter values the equilibrium solution is $Q \approx 0.2672$, which implies that $\gamma \approx 0.0591$. These parameter values place us in the unstable regions of Figures 16, 17, and 19. For these parameter values, there is a pair of complex conjugate roots of the characteristic equation with real and imaginary components $\sigma \approx 0.1728$ and $\omega \approx 4.883$. Recall that we scaled $\lambda$ by $1/\tau$ in section 4. Undoing these scalings predicts a growth rate of approximately 0.046 and an oscillation period of approximately 4.82. Initially, we filled the vessels with hematocrit very close to the appropriate steady state values. We see from Figure 20b that the oscillation period is very close to that

Copyright © by SIAM. Unauthorized reproduction of this article is prohibited.

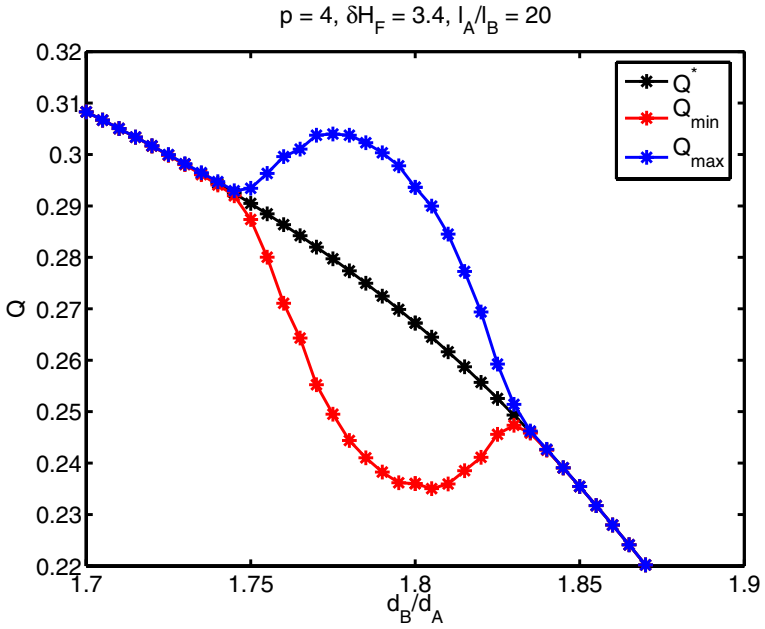


**Figure 21.** *A preliminary bifurcation diagram for changing diameter with $p = 4$, $\delta H_F = 3.4$, and $l_A/l_B = 20$. A periodic solution is initially obtained with $d_B/d_A = 1.8$, and the maximum and minimum values are shown in blue and red, respectively. The diameter ratio is then increased in increments of 0.005, the simulation is continued until the transients die off, and the minimum and maximum values are again recorded. This is repeated by decreasing the diameter ratio in increments of 0.005. The equilibrium solution is shown for reference in black.*

predicted by linear stability analysis.

We have also confirmed the existence of a finite region of instability in the $(l_A/l_B, d_B/d_A)$-plane by continuing the simulation for various values of $d_B/d_A$. In Figure 21 we plot the maximum and minimum values of the periodic solution as $d_B/d_A$ is varied. The branch of periodic solutions is created by starting at $d_B/d_A = 1.8$ and then continuing the resulting periodic solution by increasing and decreasing $d_B/d_A$. The periodic solution emerges and vanishes at values of $d_B/d_A$ which agree well with those predicted in section 6.2, and Figure 21 also suggests that the Hopf bifurcations are supercritical. We have not explored the nonlinear dynamics in detail but plan to in the future.

**7. Conclusions.** Numerous experimental studies have demonstrated that oscillations in microvascular blood flow are ubiquitous. While fluctuations in blood hematocrit and velocity are usually identified with biological control mechanisms such as vasomotion, there is evidence that oscillations may be possible in the absence of biological control. In a previous paper [5] we identified the simplest possible network, the two-node network, that could exhibit oscillatory dynamics, and we found and interpreted the three dimensionless parameters $b$, $c$, and $\gamma$ which govern the stability of equilibrium.

In this paper we develop a complete description of the roots of the characteristic equation and their dependence on the three dimensionless parameters. We show that there exists an infinite number of Hopf bifurcation curves in the $cb$-plane for a given value of $\gamma$. Using simple

Copyright © by SIAM. Unauthorized reproduction of this article is prohibited.

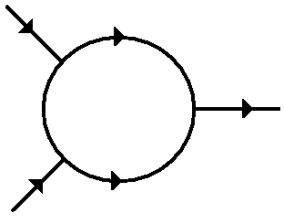

**Figure 22.** *The three-node network consists of two inlets and one outlet. One of the inlet nodes is converging, while the other is diverging. The flow in the middle branch could be in either direction.*

parametric models for the Fåhræus–Lindqvist effect and the plasma skimming effect, we map the bifurcation curves to the network parameter plane, $(l_A/l_B, d_B/d_A)$. For a given value of the plasma skimming parameter $p$ we demonstrate that there is a critical value of the Fåhræus–Lindqvist parameter $\delta$ for instability. We also show that above this threshold value there exists a finite region of instability in the $(l_A/l_B, d_B/d_A)$-plane, and we confirm these predictions with direct numerical simulation.

It is worth noting that we do not pretend that the simple parametric models provide a realistic model for microvascular blood flow. Rather, we have used these models to provide insight by making the analysis tractable. There is still some question as to the possibility of instability if we use the more realistic models of Pries et al. The major difficulty is that there is no easy way to map from the five-dimensional network parameter space, $H_F, d_F, d_A, d_B, l_A/l_B$, to the three-dimensional dimensionless parameter space, $b, c, \gamma$. For a given set of network parameters it is simple to compute $b$, $c$, and $\gamma$ and therefore determine whether the network is stable or unstable. This, however, is a rather unwieldy and unsatisfying method given the size of the five-dimensional parameter space. Our results to date indicate that instability is unlikely using the models of Pries et al., but we have no proof of this conjecture.

Even if oscillations are possible in the two-node network, the regions of instability in the network parameter space are likely to be very small. This makes the likelihood of confirming these predictions experimentally very remote. However, this parametric study does suggest several alternatives. As demonstrated by Kiani et al. [21] and Carr and LeCoin [4], oscillations are possible in larger networks. With a detailed understanding of the instability in hand, we can pursue the validation of this work in slightly larger networks. For example, we have preliminary evidence that the three-node network shown in Figure 22 has a much larger region of instability. A careful analysis of this network might pave the way for an in vitro experimental verification of these predictions.

Alternatively, we could explore other networks that are described by similar governing equations. While it is potentially difficult to find an analogy with both flow and hematocrit equivalents, we can reformulate our model into a single integral equation for the flow alone as follows. The resistance in any vessel depends on the average hematocrit $\bar{H}_i$ in vessel $i$. Since the hematocrit at any point in the vessel is determined by the inlet hematocrit at an earlier time, we can write the average hematocrit as

$$\bar{H}_i(t) = \frac{1}{l_i} \int_{t-\tau_i(t)}^{t} H_i(0,s) v_i(s)\, ds, \tag{7.1}$$

Copyright © by SIAM. Unauthorized reproduction of this article is prohibited.

where $l_i$ is the length of the vessel and $v_i(t)$ is the speed of flow in the vessel at time $t$. The time delay $\tau_i(t)$ is determined implicitly by the threshold condition,

$$\int_{t-\tau_i(t)}^{t} v_i(s)\,ds = l_i. \tag{7.2}$$

In the two-node network the flow $Q(t)$ is governed by (3.3),

$$Q(t) = \frac{R_B(\bar{H}_B(t))}{R_A(\bar{H}_A(t)) + R_B(\bar{H}_B(t))}, \tag{7.3}$$

which can now be viewed as an integral equation with two state-dependent delays since the entrance hematocrit, $H_i(0,t)$, is a function of the flow $Q(t)$ via the plasma skimming effect. Electric circuits provide an obvious analogy and may be worth investigating. In particular, the steady state $IV$-characteristic of a transistor can display *snapback* [34], which beautifully mimics the flow-pressure characteristic of blood flow in the two-node network. We hope to pursue both avenues of research in the near future.

**Acknowledgments.** We would like to thank the numerous undergraduate and graduate students at the University of New Hampshire and Olin College who have contributed in some way. These include David Cerra, Molly Goulet, Gabriel Withington, Yingyi Lao, David Gebhart, Kelly Butcher, and Keoni Mahelona. We would also like to thank Professor Mark Somerville of Olin College for his contribution regarding the voltage transfer characteristics of transistors.

## REFERENCES

[1] W. F. Ames, *Numerical Methods for Partial Differential Equations*, 3rd ed., Academic Press, New York, 1992.
[2] J. Bélair and S. A. Campbell, *Stability and bifurcations of equilibria in a multiple-delayed differential equation*, SIAM J. Appl. Math., 54 (1994), pp. 1402–1424.
[3] G. Bugliarello and G. C. C. Hsiao, *Phase separation in suspensions flowing through bifurcations: A simplified hemodynamic model*, Science, 143 (1964), pp. 469–471.
[4] R. T. Carr and M. LeCoin, *Nonlinear dynamics in microvascular networks*, Annals of Biomedical Engineering, 28 (2000), pp. 641–652.
[5] R. T. Carr, J. B. Geddes, and F. Wu, *Oscillations in a simple microvascular network*, Annals of Biomedical Engineering, 33 (2005), pp. 764–771.
[6] S. Cavalcanti and M. Ursino, *Chaotic oscillations in microvessel arterial networks*, Annals of Biomedical Engineering, 24 (1996), pp. 37–47.
[7] S. Chien, C. D. Tvetenstrand, M. A. F. Epstein, and G. W. Schmid-Schönbein, *Model studies on distributions of blood cells at microvascular bifurcations*, American J. Physiology, 248 (1985), pp. H568–576.
[8] J. W. Dellimore, M. J. Dunlop, and P. B. Canham, *Ratio of cells and plasma in blood flowing past branches in small plastic channels*, American J. Physiology, 244 (1983), pp. H635–H643.
[9] L. E. El'sgol'ts and S. B. Norkin, *Introduction to the Theory and Application of Differential Equations with Deviating Arguments*, Academic Press, New York, 1973.
[10] G. Enden and A. S. Popel, *A numerical study of plasma skimming in small vascular bifurcations*, J. Biomechanical Engineering, 116 (1994), pp. 79–88.
[11] R. Fåhræus and T. Lindqvist, *The viscosity of blood in narrow capillary tubes*, American J. Physiology, 96 (1931), pp. 562–568.

Copyright © by SIAM. Unauthorized reproduction of this article is prohibited.

[12] B. M. Fenton, R. T. Carr, and G. R. Cokelet, *Nonuniform red cell distribution in* 20 *to* 100 $\mu m$ *bifurcations*, Microvascular Research, 29 (1985), pp. 103–126.
[13] Y. C. Fung, *Stochastic flow in capillary blood vessels*, Microvascular Research, 5 (1973), pp. 34–48.
[14] L. Glass, *Synchronization and rythmic processes in physiology*, Nature, 410 (2001), pp. 277–283.
[15] L. Glass and M. C. Mackey, *From Clocks to Chaos: The Rhythms of Life*, Princeton University Press, Princeton, NJ, 1988.
[16] A. L. Goldberger, L. A. N. Amaral, L. Glass, J. M. Hausdorff, P. Ch. Ivanov, R. G. Mark, J. E. Mietus, G. B. Moody, C.-K. Peng, and H. E. Stanley, *PhysioBank, PhysioToolkit, and PhysioNet: Components of a new research resource for complex physiologic signals*, Circulation, 101 (2000), pp. e215–e220.
[17] T. M. Griffith, *Temporal chaos in the microcirculation*, Cardiovascular Research, 31 (1996), pp. 342–358.
[18] J. K. Hale and W. Huang, *Global geometry of the stable regions for two delay differential equations*, J. Math. Anal. Appl., 178 (1993), pp. 344–362.
[19] N. D. Hayes, *Roots of the transcendental equations associated with a certain difference-differential equation*, J. London Math. Soc., 25 (1950), pp. 226–232.
[20] P. C. Johnson and H. Wayland, *Regulation of blood flow in single capillaries*, American J. Physiology, 212 (1967), pp. 1405–1415.
[21] M. F. Kiani, A. R. Pries, L. L. Hsu, I. H. Sarelius, and G. R. Cokelet, *Fluctuations in microvascular blood flow parameters caused by hemodynamic mechanisms*, American J. Physiology, 266 (1994), pp. H1822–H1828.
[22] B. Klitzman and P. C. Johnson, *Capillary network geometry and red cell distribution in hamster cremaster muscle*, American J. Physiology, 242 (1982), pp. H211–H219.
[23] A. Krogh, *The Anatomy and Physiology of Capillaries*, Yale University Press, New Haven, CT, 1922.
[24] A. Krogh, *Studies on the physiology of capillaries:* II. *The reactions to local stimuli of the blood-vessels in the skin and web of the frog*, J. Physiology, 55 (1921), pp. 414–422.
[25] J. M. Mahaffy, P. J. Zak, and K. M. Joiner, *A geometric analysis of stability regions for a linear differential equation with two delays*, Internat. J. Bifur. Chaos Appl. Sci. Engrg., 5 (1995), pp. 779–796.
[26] F. Mollica, R. K. Jain, and P. A. Netti, *A model for temporal heterogeneities of tumor blood flow*, Microvascular Research, 65 (2003), pp. 56–60.
[27] D. Parthimos, K. Osterloh, A. R. Pries, and T. M. Griffith, *Deterministic nonlinear characteristics of in vivo blood flow velocity and arteriolar diameter fluctuations*, Physics in Medicine and Biology, 49 (2004), pp. 1789–1802.
[28] A. S. Popel and P. C. Johnson, *Microcirculation and Hemorheology*, in Annual Review of Fluid Mechanics. Vol. 37, Annu. Rev. Fluid Mech. 37, Annual Reviews, Palo Alto, CA, 2005, pp. 43–69.
[29] A. R. Pries, K. Ley, and P. Gaehtgens, *Red cell distribution at microvascular bifurcations*, Microvascular Research, 38 (1989), pp. 81–101.
[30] A. R. Pries, D. Neuhaus, and P. Gaehtgens, *Blood viscosity in tube flow: Dependence on diameter and hematocrit*, American J. Physiology, 263 (1992), pp. H1770–H1778.
[31] A. R. Pries, T. W. Secomb, T. Gessner, M. B. Sperandio, J. F. Gross, and P. Gaehtgens, *Resistance to blood flow in microvessels in vivo*, Circulation Research, 75 (1994), pp. 904–915.
[32] G. P. Rodgers, A. N. Schechter, C. T. Noguchi, H. G. Klein, A. W. Niehuis, and R. F. Bonner, *Periodic microcirculatory flow in patients with sickle-cell disease*, New England J. Medicine, 311 (1984), pp. 1534–1538.
[33] S. P. Sutera and R. Skalak, *The history of Poiseuille's law*, in Annual Review of Fluid Mechanics. Vol. 25, Annu. Rev. Fluid Mech. 25, Annual Reviews, Palo Alto, CA, 1993, pp. 1–19.
[34] S. H. Voldman, *ESD: Circuits and Devices*, John Wiley and Sons, New York, 2006.
[35] C. Wiederhielm, J. W. Woodbury, S. Kirk, and R. F. Rushmer, *Pulsatile pressures in the microcirculation of frog mesentery*, American J. Physiology, 207 (1964), pp. 173–176.
[36] K. P. Yip, N. H. Nolstein-Rathlou, and D. J. Marsh, *Chaos in blood flow control in genetic and renovascular hypertensive rats*, American J. Physiology, 261 (1991), pp. F400–F408.

Copyright © by SIAM. Unauthorized reproduction of this article is prohibited.